THEORY AND APPLICATIONS OF ABSORBING GUIDED-MODE RESONANT DEVICES IN SENSING, COMMUNICATIONS, AND DISPLAY

by

ALEXANDER LEIGHTON FANNIN

DISSERTATION

Submitted in partial fulfillment of the requirements
for the degree of Doctor of Philosophy at
The University of Texas at Arlington
August, 2017

Arlington, Texas

Supervising Committee:

Robert Magnusson, Supervising Professor
Kambiz Alavi
Michael Vasilyev
Yuze Sun
Brett Wenner

ACKNOWLEDGMENTS

This work was supported by the KBRwyle Laboratories, Inc. with Contract No. FA8075-14-D-0025-0005. I am thankful for the funding support through AFOSR Lab Task 14RY15COR (PO: Dr. G. Pomrenke).

I thank the Air-Force Research Lab (AFRL) for its funding and support including Dr. Brett Wenner, Dr. Monica Allen, and Dr. Jeffery Allen.

I am deeply appreciative for the guidance and support provided by my supervisor, Dr. Robert Magnusson, who provided the necessary materials and insight which made this document possible.

I am further grateful for my supervising committee comprised of Dr. Kambiz Alavi, Dr. Michael Vasilyev, Dr. Yuze (Alice) Sun, and Dr. Brett Wenner and all of the support and recommendations they have provided in the preparation of this research.

I would like to express my thanks to the staff at the UTA nanofab whom helped to train and guide my actions for various processes and equipment.

Lastly, I am thankful to Dr. Kyu Lee who assisted in the fabrication and investigation of several of the earliest designs in my work.

DEDICATION

I would like to dedicate this work first and foremost to my supervising professor, Dr. Robert “Meta” Magnusson, the final boss before acquiring one’s Ph.D. I hope your tomatoes always grow strong, and the armadillos leave you in peace.

Next, I would like to give my thanks to my wife to whom I have dedicated my life and its fruit. You will always be my gazoofus. It is my sincerest hope that I can one day give you the support you have granted me all of these years.

To my mother, I hope only that I become the retirement plan you always wanted. To my father, I hope that I can be the retirement plan your wife always wanted. To my grandfather, who inspired me to pursue this path in life, I say thank you, you have made this possible. To my late grandmother, I wish only that you had had the chance to see this.

I would also like to thank many of the colleagues I have amassed including Manoj Niraula, David Winarski, Han Zhang, Hafez Hemmati, and Daniel Carney amongst many others.

Lastly, I would like to thank the many friends I have accumulated who have stood by me all of these years with a special thank you to Jason Doerr, Justin Parks, Joshua Guhl, Zach McLain, and Kyle McLain. I’m finally, probably, maybe not who knows, almost done.

Table of Contents

List of Illustrations

List of Tables

List of Abbreviations

Amorphous silicon – a-Si
Anti-reflection – AR
Atomic force microscope – AFM
Coherent perfect absorption – CPA
Deep reactive ion etching – DRIE
Effective medium theory – EMT
Fabry-Perot – FP
Full width half maximum – FWHM
Guided mode resonance – GMR
Laser interferometric lithography – LIL
Particle swarm optimization– PSO
Photoresist – PR
Reactive ion etching – RIE
Rigorous coupled wave analysis – RCWA
Scanning electron microscope – SEM
Surface plasmon resonance – SPR
Type II super lattice – T2SL
Total internal reflection – TIR
Transverse electric – TE electric-field vector is normal to the plane of incidence
Transverse magnetic – TM electric-field vector lies in the plane of incidence
1D – One-dimensional
2D – Two-dimensional

ABSTRACT

THEORY AND APPLICATIONS OF ABSORBING

GUIDED-MODE RESONANT DEVICES IN

SENSING, COMMUNICATIONS,

AND DISPLAY

Alexander Leighton Fannin, Ph.D.

The University of Texas at Arlington, 2017

Supervising Professor: Robert Magnusson

Guided-mode resonant (GMR) technology is incorporated into lossy dielectric materials to assist in the absorption of incident light for various applications. Varying topologies and methodologies are explored. A series of devices taking advantage of narrow band, coherent interferometry is found to work as a serviceable coherent perfect absorber (CPA) whereby the total transmittance through the device is tunable based upon the relative phase of two or more beams. The differing beams are shown to be exciting the same mode in the device enabling the interferometric function. A similar, active topology for use in electronically interrogable interfacing is explored. Multiple hybrid metal-

dielectric topologies are explored combining function from GMR, plasmonics, and Rayleigh anomaly to create various filters, sensors, and displays. Among these, a low index sensor topology is found to be operable between the cover and substrate Rayleigh wavelengths. Wideband absorptive properties utilizing GMR and 2D expansion are investigated. It is found that 1D, wideband, polarization sensitive devices can be straightforwardly extrapolated into 2D-patterned polarization insensitive ones. Ultra-sparse absorptive gratings enabled by a form of vertical coupling and assisted via GMR are shown to have polarizing attributes with extinction ratios theoretically in excess of 10^8:1 with low reflection. Lastly, basic absorbing GMR design principles are extrapolated into the Mid IR illustrating comparable performance, in theory, to dielectric absorbers enhanced by plasmonic effects.

Chapter 1

Introduction

1.1 Basic history and development of GMR

Optical devices and their applications have been of interest for thousands of years dating back to Egypt in 1900 B.C. and perhaps earlier [1]. The earliest optical devices of interest were items like mirrors that were often made of polished copper and bronze to enable a crude reflection. Since that time the field of optics has expanded considerably to include devices and technologies the Egyptians couldn't have even comprehended like telescopes and lasers. A recent technology developed in the past thirty years is the use of guided-mode resonance (GMR) effect otherwise known as leaky-mode resonance effect. Grounded in fundamental early studies [2-4] GMR technology was proposed for potential applications in the early 1990's for example for optical filters [5,6]. It has gone on to be of interest in sensing [7-9], energy collection [10], laser applications [11], and more. In short, GMR devices operate as periodic thin films; related 1D or 2D devices are often called waveguide gratings. To guide light by total internal reflection (TIR), the effective refractive index of the guiding structure must be sufficiently higher than that of the cover or substrate. A wide variety of design configurations are available with many suitable

materials to be chosen by design. Figure 1.1 illustrates a one device architecture that is often used for GMR grating devices.

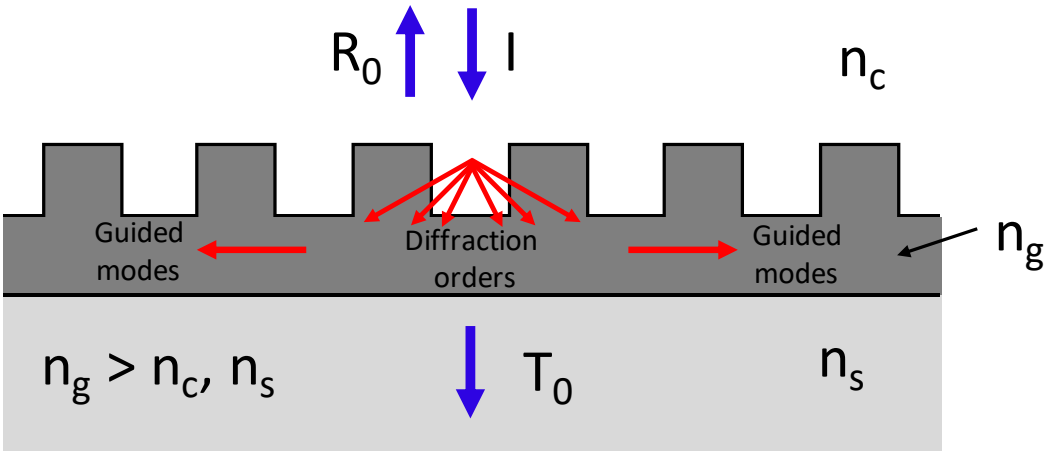

Fig. 1.1 - Illustration of a characteristic GMR structure with normally incident light. Diffraction orders are shown to guide temporarily before being reradiated back out. The relationship of the guiding layers refractive index (n_g) to the cover (n_c) and substrate index (n_s) is shown.

1.2 Designing GMR elements

While GMR devices have been of considerable interest over the past several decades they pose several challenges on how to find suitable topologies for various tasks. Efficient theoretical and analytical methods are available for design. Moreover, there are many computerized methods for exploring various topologies including rigorous coupled wave analysis (RCWA) [12], finite domain time difference (FDTD) [13], and finite element methods (FEM) [14]. Each of these methods can be used to estimate the response of a GMR-based device assuming different materials, critical dimensions, etc. That said, RCWA is generally the fastest and most utilized method due to its simplicity. It has been

experimentally confirmed to be exceedingly accurate, particularly, at detecting GMR peaks. The majority of calculations conducted in this document have been done with RCWA.

Each of the presented techniques can determine the response of a given structure. However, for forward optimization this can still prove quite tedious as even thousands of calculations are no guarantee that a desirable topology will be found. To further assist in the discovery of desirable devices the use of particle swarm optimization (PSO) can be of considerable aid [15]. PSO codes work by taking a set of parameters, each with a user specified range, and assigning a random value for each parameter. An individual set of parameters is called a particle. Prior to running the code, the user may determine how many particles exist within the system. The code will then interact with a computational method of the users choice, like RCWA, and evaluate each particle containing its set of random parameters. The results are compared to a user defined result that resembles an ideal device for a given application. Particles that return results that are a good match for the desired spectrum will remain relatively close to their current parameter set. Particles that return unfavorable results will make relatively larger changes to their parameter set and slowly begin to migrate towards particles with more favorable results. In the end, if an acceptable solution exists, it has been shown that using inverse methods such as PSO can considerably reduce the required time and

computational resources for discovering desired topologies. Many of the topologies that will be discussed in this document have been obtained or enhanced using PSO.

1.3 Fabrication of GMR elements

There are many avenues available for fabricating GMR devices including e-beam lithography, traditional mask lithography, and interference lithography or laser interference lithography (LIL). Of these, e-beam is by far the most customizable option available enabling, in theory, complete customization of an entire device. While attractive, e-beam lithography does have some sizeable drawbacks. The biggest of these is the inherently slow rate at which devices can be manufactured. The process in completely linear requiring the beam to write each feature individually. Furthermore, large structures may suffer from stitching errors for large device areas, often being limited to 1 square millimeter. Traditional masks offer some advantages over e-beam lithography. Most notably, they can be scaled to process entire wafers in parallel saving time. However, masks are unalterable implying for each new design, a new mask may be procured. In short, masks are highly desirable for mass production processes, but have more limited uses in research. The last option that will be discussed is LIL. LIL enjoys a mix of benefits from the two processes described above but comes with its own disadvantages. One advantage of LIL is its scalability. Namely, like traditional lithography, the exposed area can be scaled as necessary to accommodate larger or smaller devices. Additionally,

through the inclusion of an adjustable mirror stage, the periodicity of an exposed device can be altered via computer without the need of additional masks. One disadvantage of LIL is that for any single exposure, the features will be repeated without customization. Additionally, the UV source must be a high quality laser in order to ensure coherency of the interfering beams. The majority of devices featured in this document were fabricated using LIL. Figure 1.2 offers a basic overview of the preferred GMR fabrication process used in the majority of this document.

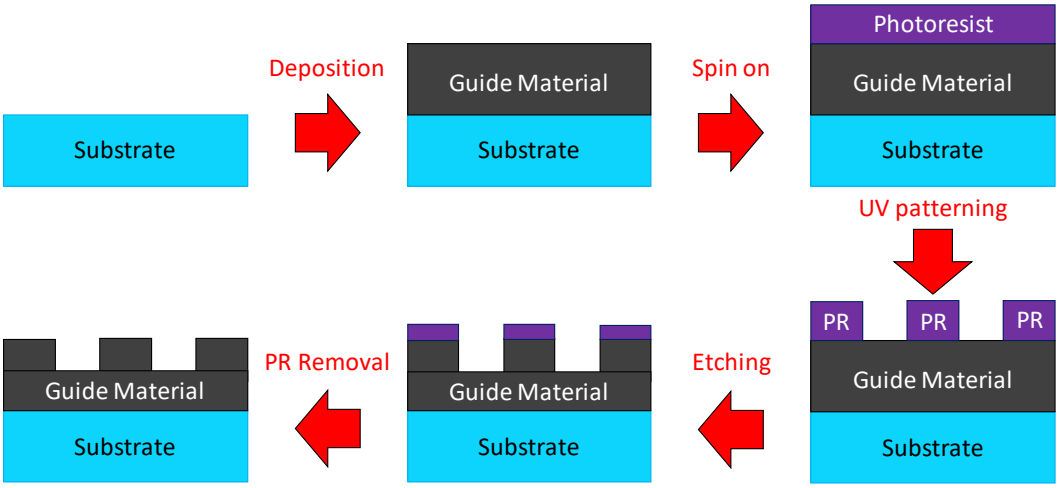

Fig. 1.2 - Standard process for fabricating zero-contrast GMR elements using LIL.

1.4 Absorption in GMR

In this dissertation, many resonant structures are investigated with an emphasis on enhancing or utilizing absorption. In general, absorption is either minimized, in devices like waveguides and mirrors, or maximized, in devices like solar cells and photodetectors.

Perhaps best described as a method for imparting energy to matter from light, absorption can be a very useful feature of a resonant system. In most GMR devices absorption is undesirable and many materials are chosen based upon their absorption coefficient at the required wavelength. As such, many simulations are performed with the assumption of a lossless material to further simplify the simulation. In many cases, this practice is perfectly acceptable and does not strongly differ from what is found in fabricated devices. However, for high Q-factor systems and materials with even marginally high absorption coefficients this can cause the calculation to return a significantly erroneous answer. Amorphous silicon (a-Si) is an excellent example of a material with a marginal absorption coefficient that can surface quite drastically during resonant conditions. Figure 1.3 illustrates such an example.

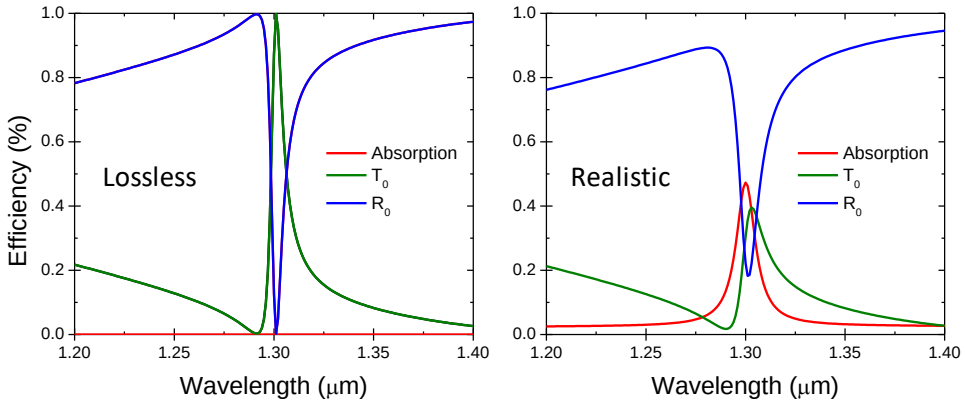

Fig. 1.3 - Comparative performance of a lossless simulation to a more realistic one illustrating the importance of including absorption coefficients within a simulation.

1.5 Topics presented in this work

In this document, GMR structures will be utilized with a strong emphasis on absorption. Topics including coherent perfect absorption (CPA), hybrid metal-dielectric structures, and wideband absorption will be addressed as well as absorptive, polarizing optics and Mid IR GMR devices for sensing applications. CPA, originally proposed by Stone et. al [16], is traditionally achieved by utilizing a slab waveguide and tuning it to specific wavelength. This topology is somewhat limited as only one angle, normal incidence, can be utilized and an individual device can only cater to a single wavelength. GMR based CPA grants the designer much more freedom including operating angle and a selection of wavelengths. Mixed metal-dielectric topologies offer many interesting possibilities including the marriage of GMR and surface plasmon resonance (SPR) operating in unison to create various devices like filters [17] and sensors [18]. Surface plasmon resonance is a special condition that occurs on the interface between a conductor, usually a metal, and a dielectric. In short, when an incident photon's frequency and momentum match that of a surface plasmon polariton (SPP) then the incident photon can excite a SPP. In order to match a photons momentum to that of a SPP it is necessary to use a dielectric medium, often a prism [19]. In general, only TM polarized light can excite a SPR. SPR is often detected using absorption. The requirement of a dielectric to be present to form a SPR creates an opportunity to mix the effects with GMR. Wideband absorbers are of considerable interest for devices like detectors and solar panels. While several GMR

based topologies have been discussed for such applications this document will present additional information and possible ideas for expanding the role they play. Specialized grating topologies assisted by GMR can be shown to have highly desirable polarizing properties. Theoretically, extinction ratios as high as 10^{19}:1 can be achieved in a device that reflects less than 10% of the incident light. This document will discuss the possible applications and advantages of such systems. Lastly, GMR absorbers can be demonstrated in the Mid IR with direct comparison to plasmonic assisted devices. This document will briefly touch upon the feasibility of scaling these resonant effects into the Mid IR to demonstrate their continuing capabilities in the Mid IR region.

Chapter 2

Coherent perfect absorption in guided-mode resonant thin films

2.1 Introduction

Absorption is one of the most fundamental processes that occurs when light interacts with matter. Engineering absorption is applied to practical application such as detection, laser scribing, and energy generation. The ability to control absorption in low dimensional material systems such as thin-film geometries is an important and flourishing field of study. In solar energy applications, wideband absorption of incoherent unpolarized light is essential. In that context, Yoon et al. demonstrated a 1D periodic amorphous Si thin-film grating structure that absorbs almost 90% of fully conical unpolarized light across the entire visible spectrum [1]. Cheng et al. realized a 2D periodic silver structure that exhibited nearly perfect absorption of incoherent light by plasmonic resonance in the visible spectral region [2]. Recently, techniques implementing absorption under coherent light interference have gained considerable attention due to several advantages including the use of linear optics and novel functionality not attainable by other means. Thus, the coherent perfect absorber (CPA) concept was proposed by Chong et al. to achieve photonic resonance in semiconductor Fabry-Pérot cavities [3]. At about the same time, it was shown by theoretical analysis of a metal

grating undergoing plasmonic resonance that total absorption is obtainable in a multiport system by properly configuring input coherent light waves at critical coupling [4]. In ideal CPA devices, two or more input waves totally couple to a single-resonance state and undergo perfect absorption by the intrinsic loss associated with that state. Thus, it was found that complete absorption can be achieved using multiple beams incident on a lossy device such that interference of outgoing beams results in zero outgoing power [3], [4]. As coherent absorbers do not require nonlinear effects to actively modulate light intensity [5], they can be used as low-power active devices such as compact optical switches, modulators, and light-electricity transducers [3-7].

CPA has been demonstrated experimentally in flat silicon films [7], periodic metals by surface-plasmonic resonance on a silver grating [8], and in microring resonators [9]. It has also seen exposure in graphene thin films [10], and bilayer structures [11]. Recently, we proposed an alternate approach to CPA in which periodic films are applied. Specifically, we modeled resonant silicon gratings and showed that these are effective in CPA applications [12]. Here, we provide experimental evidence to support these theoretical predictions.

2.2 Experiments

The experimental results presented apply the guided-mode resonance (GMR) effect as a new basis for coherent perfect absorption. In summary, guided-mode

resonance effects arise via quasi-guided, or leaky, waveguide modes induced on patterned films with subwavelength periods [13-17]. Simple GMR structures comprising a single one-dimensional (1D) periodic layer have been used to create filters, polarizers, and polarization-independent devices with applications in biosensing, communications, and solar cell enhancement [18-20]. Similarly, the GMR concept can easily be adapted into two-dimensional (2D) structures to offer further advantages in each of these applications [21-23]. To achieve coherent perfect absorption within a GMR device it is necessary to implement interaction of multiple coherent beams entering the device. The structure of the device determines the wavelengths that are coupled and the angles of coupling. When multiple coherent beams are coupled to the same mode they inherently interfere with one another. This interference can be perfectly constructive, perfectly destructive, or somewhere in-between depending on the phase between two or more beams. In the case of two beams, the phase of one beam can remain fixed while the other one is varied to effectively change the interference interaction. This is the key concept in our design.

Figure 1.1 shows the structure of the proposed GMR-based CPA device. The beams labeled I_1 and I_2 are subject to phase control. While it is possible to create any amount of phase difference between 0 and 2π, we address two particular cases where both beams are perfectly in phase or perfectly out of phase. The CPA state occurs as two resonant guided modes separately excited by I_1 and I_2 constructively interfere. Modal

energy flowing along the layer is absorbed by the intrinsic loss of the material. This is the ordinary absorption mechanism encountered in a medium with a complex index of refraction $n_d = n + ik$ where the imaginary part k is non-zero. Conversely, when the beams are perfectly out of phase, there results destructive interference and effective scattering of the input waves with minimal absorption being possible. These two cases represent nearly perfect absorption and nearly perfect transmission, respectively. Furthermore, it is possible to truncate the level of transmission through the manipulation of the phase. CPA, unlike conventional incoherent absorption, has the added benefit of tunability in the response whereby the resulting output can be modulated using light as control. Absorption can also arise from scattering by rough device surfaces. Atomic-force microscopy (AFM) is employed on our fabricated samples to reveal minimal surface roughness; hence we believe that loss by this mechanism is negligible.

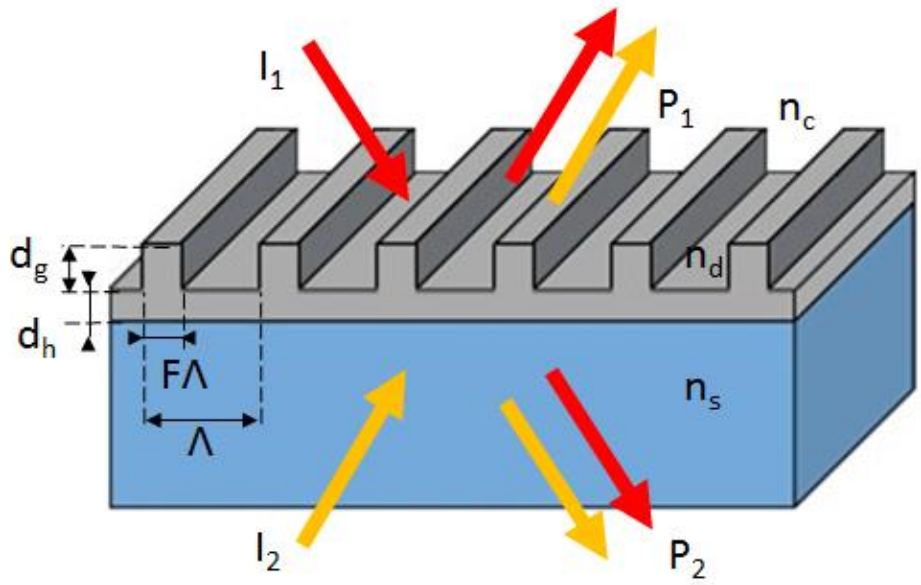

Fig. 2.1 - Architecture of a GMR-based CPA device including key parameters. Ports I_1 and I_2 represent the input beams while P_1 and P_2 represent output ports. Here, d_g is grating depth, period is Λ, fill factor is F, and the homogenous sublayer thickness is d_h.

We aim to realize a GMR CPA element resonating at λ = 1300 nm with a 45° incidence of TM-polarized light. Applying numerical design methods, we arrive at a parameter set with a period of 474 nm, a fill factor of 0.26, sublayer thickness of 175 nm, and a grating height of 94 nm assuming $n_d = 3.589 + i0.0127$ for the index of refraction measured by ellipsometry and assuming $n_c = 1$. The devices applied in this research are strongly spatially modulated. The spatial modulation strength is defined as $\Delta\varepsilon = n_d^2 - n_c^2 = 11.881 + i0.0912$. In such strongly modulated devices the transverse leakage out of the illuminated spot is minimal. The device area for all of our fabricated structures is 5mm by

5mm. The illuminated spot diameter is approximately 1mm; thus the spot is well surrounded by the periodic medium. As indicated in Fig. 2.1, the design consists of amorphous silicon (a-Si) on a SiO_2 substrate. These materials are chosen for their optical properties, wide availability, and simple deposition procedures. Different materials can be used to tailor the characteristics of the device as needed for any specific spectral region.

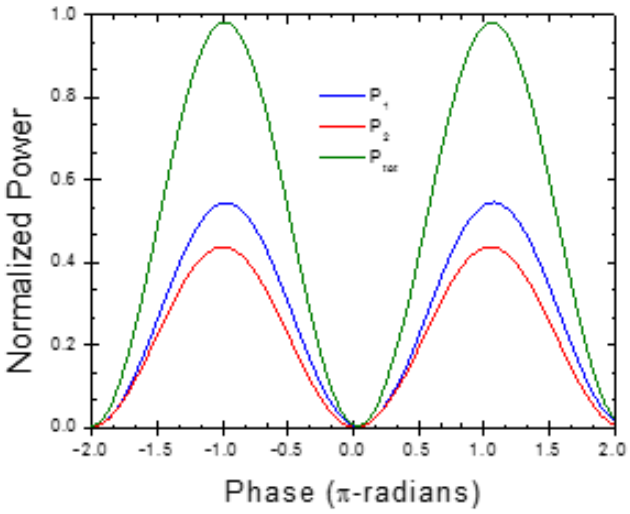

Fig. 2.2 - Theoretical device performance at 1300 nm wavelength assuming TM polarization. The x-axis represents the phase difference between the two input beams assuming perfect phase matching at the zero mark. This design assumes an even distribution of power between beams I_1 and I_2.

Figure 2.2 shows a theoretical prediction of device performance at 1300 nm under TM polarization in which the electric-field vector is parallel to the plane of incidence. It illustrates the phase-sensitive outgoing powers that include the two extreme cases with nearly perfect absorption observed at –2π, 0, and 2π radians and near perfect

transmission observed at –π and π radians. The absorption state at the phase difference of 0 yields the minimum total outgoing power of ~1 % while the transmission state at the phase π shows a maximum of ~98 %.

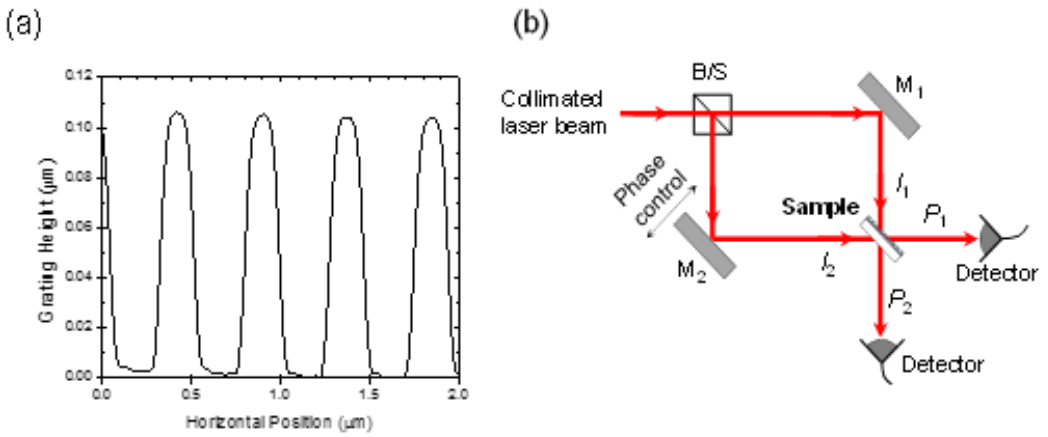

Fig. 2.3 - (a) AFM profile of a fabricated prototype device. (b) Experimental setup to demonstrate CPA. A piezoelectric stage enables phase control of one beam. The axis of displacement for the piezoelectric stage is parallel to the incident beam from the beam splitter.

The experimental prototype consists of a single layer of a-Si deposited on a glass substrate. A spin-coated photoresist layer is patterned by UV holographic lithography. The a-Si is partially etched, using the developed resist as a mask, to create the grating structure. We characterize the fabricated device with atomic force microscopy with results shown in Fig. 2.3(a). We find that that the fabricated prototype has a period of 474 nm, fill factor of 0.24, and grating height of 103 nm. An additional scanning electron microscope analysis yields sublayer thickness of 164 nm. Angular measurement confirms

that a resonance peak at 45° occurs at λ = 1266 nm with this prototype device. Figure 2.3(b) shows a simplified diagram of the experimental setup used to test the device. A 50/50 beam splitter is used for this experiment. Thus the present design operates at a 1:1 power ratio. The experiment also utilizes an in-line polarizer, a fiber-to-free-space collimator, and a free-space Glan-Taylor polarizer not shown in Fig. 2.3. The use of both the Glan-Taylor and the in-line polarizer ensures maximum available power for the desired polarization. The sample is mounted on a computer-controlled high-resolution rotation stage for alignment. To account for hysteresis errors in the piezo-electric stage, the data is recorded using ascending voltage values subsequently correlated to displacement. Similar to the rotation stage, the piezo-electric stage is computer controlled.

2.3 Results

Figure 2.4(a) compares theoretical and experimental results for the prototype device. The theoretical model applies the experimental parameters of the fabricated device. It is found that the total power leaving the GMR device in the full-scattering state is ~99% as seen in the figure. This is close to the ideal case of 100%. In the full-absorption state, the scattered power is at ~22%, deviating considerably from the ideal value of zero. We note that these are initial experimental results and thus the fabricated device does not presently achieve strictly perfect absorption. The reason for the deviation is primarily

due to the fact that the laser beams used here have Gaussian profiles and differ considerably from the ideal plane waves with flat phase fronts assumed in the analysis of resonant absorption. We expect that improved collimation of the input beams will lead to results close to the ideal predictions. Additionally, there is some noise in the data as visible in the experimental curves in Fig. 2.4(a). The noise is mainly due to the high sensitivity of the interferometric optical setup to mechanical vibrations.

As a reference, in the exact same experimental configuration, we substitute the periodic device with a flat layer of a-Si has the same total thickness as the fabricated GMR prototype. The results appear in Fig. 2.4(b). There is a dramatic difference observed for these two cases. As seen in Fig. 2.4(b), in stark contrast to the GMR case, there is very minimal absorption as the input power is nearly fully scattered independent of the phase. The fluctuations in Fig. 2.4(b) account for less than 10% change in the overall power leaving the system. In both cases, no detectable amount of power is measured leaving the system through the sides of the device.

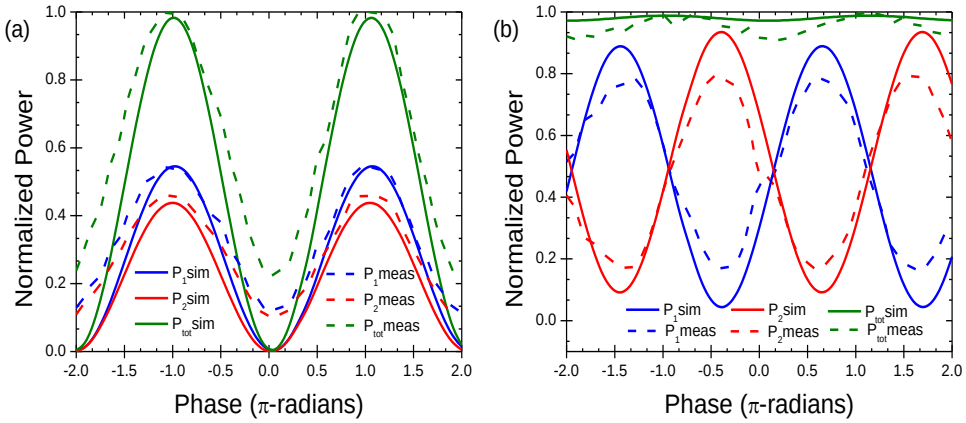

Fig. 2.4 - (a) Measured device performance compared to simulated performance at λ = 1266 nm under TM polarization. (b) Measured data from the same experiment using a thin film of amorphous silicon with the same thickness and complex refractive index as the device used in part (a).

As the resonantly absorbed power is highly dependent on the phase-sensitive internal field intensity associated with the excited guided mode, it is of interest to examine this point in some detail. A resonance with a high quality factor generally implies strong internal fields and extended photon lifetime which in turn exposes the light to the weakly absorbing material longer, thereby enhancing the absorption. Figure 2.5 compares the simulated device to the measured results across the band as well as the computed internal magnetic field profile of the fabricated device under illumination of a single beam at 45° with λ = 1266 nm. The scale is set relative to the amplitude of the incident excitation wave assumed to have unit amplitude. There is clearly strong resonant

buildup of energy within the device. We note moreover that the resonant mode has the shape of the fundamental TM_0 waveguide mode and resides maximally in the sublayer.

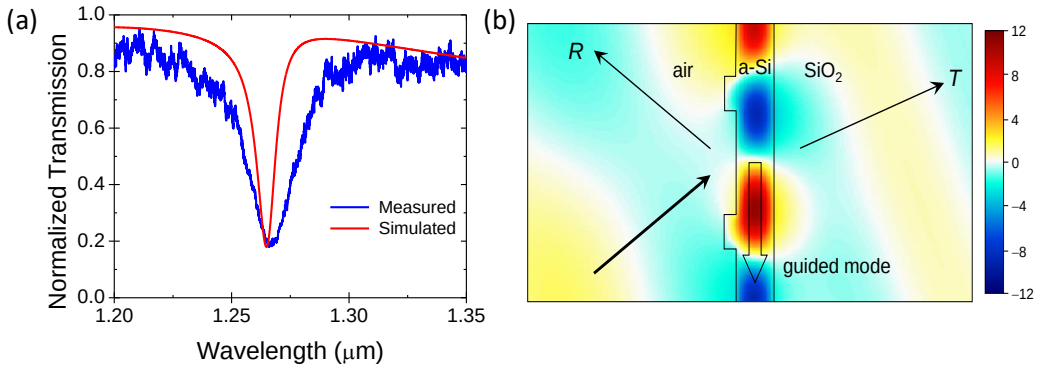

Fig. 2.5 - (a) Comparison of simulated and measured device performance under single beam excitation at 45 ° incidence. (b) Simulated internal magnetic fields using the parameters of the fabricated device.

Figure 2.5(a) illustrates the fundamental response of the device. There is a finite operating bandwidth with a FWHM of approximately 10 nm according to the simulation data. It is within this spectral bandwidth that the proposed absorption can occur. However, we note that the complex refractive index varies slowly with wavelength. Therefore, it is possible to design these elements to operate at different central wavelengths. The coherent absorption could thus be shifted to a different spectral location but again the bandwidth would be defined by the device parameters.

2.4 Conclusions

In summary, we presented experimental results illustrating the viability of coherent perfect absorption under guided-mode resonance in nanopatterned thin films

with residual, albeit small, loss. Significant levels of resonant in-phase absorption and nearly-perfect out-of-phase scattering are shown. These results are contrasted with the absorption and scattering properties of equivalent unpatterned films where only minor absorption is realized for all values of relative phase. Improved experimental conditions implementable by laser beam conditioning are expected to yield experimental data close to the ideal CPA state.

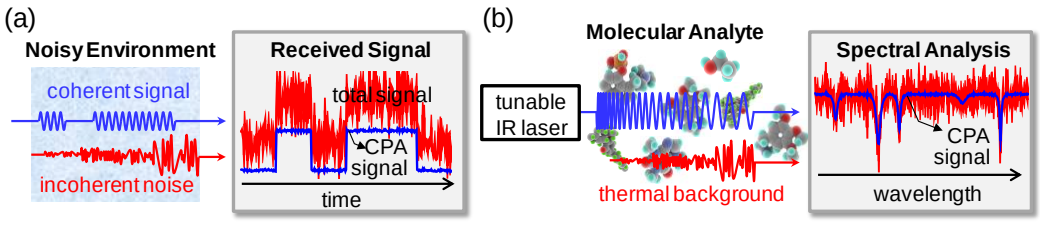

Fig 2.6 - Potential applications of CPA as a coherent signal filter. (a) Noise suppression in telecommunication signal receivers. (b) Thermal-background-free infrared spectroscopy.

Noise suppression in optical communications and spectroscopic material analysis is a possible application of the GMR CPA effect. As conceptually illustrated in Fig. 2.6(a), with a CPA photodetector, noise can potentially be filtered by the detector itself without any special noise elimination schemes. Moreover, infrared (IR) spectrometers are important for material composition analysis and hazardous material detection as most molecular species have their own vibrational fingerprints in the IR domain. Thermal background noise can be intense in normal environments at room temperature, and an analyte sample itself can act as a strong noise source for IR spectroscopy. This incoherent noise can be filtered by a CPA-integrated photodetection method as schematically

depicted in Fig. 2.6(b). Further study on GMR-CPA integration with existing semiconductor devices may produce novel active optical devices such as optical-to electrical/electrical-to-optical modulators and compact optical amplifiers with a laser diode in CPA configuration.

Chapter 3

Properties of mixed metal-dielectric nanogratings for application in resonant absorption, sensing, and display

3.1 Introduction

Many advanced device concepts in nanoplasmonics and nanophotonics are grounded in intricate resonance effects generated with nanopatterned films. As incident light couples to the film, characteristic resonance features impose spectral signatures on the output light. The guided-mode resonance (GMR) concept refers to quasi-guided, or leaky, waveguide modes induced in periodic layers; this effect is primarily associated with low-loss dielectric media. In contrast, the surface plasmon resonance (SPR) concept is associated with metals and appears as an electromagnetic field charge-density oscillation at the interface between a conductor and a dielectric. These foundational resonance effects constitute a wide basis for applications and have therefore been of interest for decades across the globe. Typically, in the technical literature, each effect is treated individually with only a limited body of knowledge on devices supporting these effects in unison.

As a fundamental phenomenon, the guided-mode resonance effect has been known for a long time [1-7]. However, only relatively recently has it been proposed for useful devices [6,7]. This device class, with thickness and period on the order of the wavelength, yields compact elements exhibiting a plethora of varying photonic spectra. Applying powerful electromagnetic design methods, the spectral bands of these subwavelength resonant leaky-mode elements can be engineered to achieve photonic devices with practical attributes. For example, a single periodic layer with one-dimensional periodicity enables narrow-line filters, polarizers, reflectors, and polarization-independent elements [8]. When used as mirrors or filters they can be tailored for both wideband and narrowband operation while incorporating polarization sensitivity or insensitivity. In practice, they currently find most use in refractive index and biological sensing [9-12].

Plasmonic resonance effects are the basis for a large body of literature including several books [13-15]. The origin of their observation dates back more than 100 years if the early experimental results by Wood [16] are interpreted as being due to plasmonic resonances [17]. Plasmons can be localized with SPRs arising on small structures or appear as propagating waves along metal-dielectric interfaces often called surface-plasmon polaritons in that case. Indeed, SPR effects are far better known than GMR effects as measured by publication activity in the

literature. Theoretically and experimentally, an SPR is invoked by transverse-magnetic (TM) polarized light and couples to the interface at a specific wavelength and at a specific angle creating an absorptive dip in reflection or transmission [13]. SPRs have been proposed to enhance various types of devices including sensors [18-20], solar cells [21], and displays [22].

The aim of this chapter is to investigate the feasibility and potential utility of a class of optical devices based on hybridizing these two well-known photonic resonance effects. Specifically, sensors containing metals and dielectrics enable cooperative resonance effects based on simultaneous leaky modes and surface-plasmon polaritons. Whereas ordinary SPR sensors allow only a single polarization state, the incorporation of guided-mode resonance capability enables dual-polarization sensing with a resulting hybrid sensor device. In fact, as dielectric-metal systems support multiple modes for each polarization state, multiple individual and mixed SPR/GMR resonance locations can be monitored. Analogous interesting uses addressed here are in absorbers and display pixels.

The body of available results on the properties of such hybrid systems is limited. In the past, mixed GMR-SPR devices have been utilized in displays [22], to strengthen surface-enhanced Raman spectroscopy (SERS) [23,24], and to create

hybrid waveguide structures [25-29]. Initial results on hybrid sensors have also been previously presented by our group [29].

3.2 Example hybrid SPR/GMR structures

An elementary guided-mode resonator consists of a subwavelength dielectric grating on top of a homogenous layer. Figure 3.1(a) illustrates a particular grating topology with periodicity (Λ) = 500 nm, grating thickness (d_g) = 600 nm, fill factor (F) = 0.5, refractive index of the grating (n_g) = 2.5, the substrate (n_s) = 1.5, and the cover (n_c) = 1.33. The resulting spectral response to normally incident light for both TE and TM polarizations was calculated using rigorous coupled-wave analysis (RCWA) [30] and is shown in Figs. 3.1(b-c). There are four resonance peaks in the chosen spectral band; two each for TE polarization and TM polarization. In this simulation, the grating elements are lossless, T_0 and R_0 are complements in both polarization states for wavelengths longer than the Rayleigh wavelength at which the ± 1 diffraction orders are cut off. The addition of the 10 nm gold layer in Fig. 3.1(d) breaks up the symmetry observed in Fig. 3.1 (a). Further, constant refractive indices are assumed for the dielectrics and wavelength dependent dispersion data from Johnson and Christy is used for the gold layer [31].

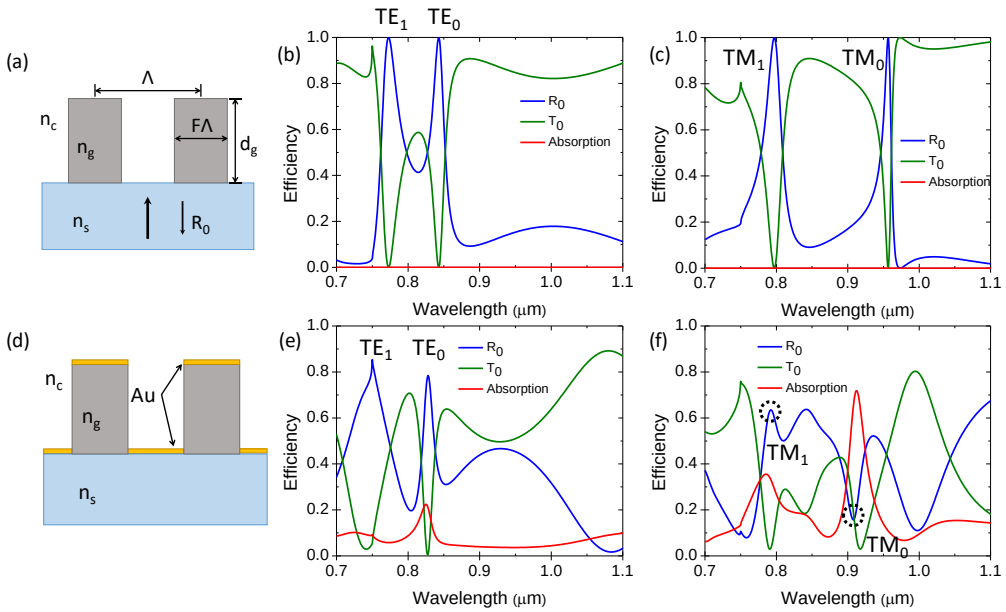

Fig. 3.1 - (a) Topology used in the study where Λ = 500 nm, d_g = 600 nm, F = 0.5, n_g = 2.5, n_s = 1.5, and n_c = 1.33. (b) Zero-order reflectance, transmittance, and absorption spectra for TE-polarized incident light for the model shown. (c) Same as (b) for TM-polarized light. (d, e, f) Same as (a, b, c) with a 10 nm thick Au layer as shown. Here, TE (TM) polarization refers to incident electric field (magnetic field) vector being along the grating grooves.

Since SPR effects are induced by TM polarized light, we do not expect strong absorption to occur under TE-polarized light as confirmed in Fig. 3.1(e). In general, the absorption is low but builds slightly near the TE GMR resonant peaks. This increase in absorption for the TE state is not a plasmonic effect. The GMR conditions concentrate energy within the grating and trap the light effectively forcing it to remain in the structure thus exposing it to the absorptive gold layer. Similar phenomena can be observed in GMR devices composed of moderately lossy materials whereby an absorption peak is observed under resonant

conditions. Therefore, we find that the resonant properties of the dielectric grating device and the hybrid device are qualitatively similar for TE-polarized light. Figure 3.1(f) illustrates the hybrid device under TM polarized light experiencing combinational GMR and SPR effects at 785 nm and 912 nm. As shown in Fig. 3.2, the resonance at 785 nm is associated with a TM_1 mode while the resonance at 912 nm corresponds to a TM_0 mode. The TM_0 mode has a narrower linewidth than the TM_1 mode implying a higher Q-factor which in turn traps the light for longer duration allowing the gold to absorb more energy both intrinsically and in the form of a SPR. Figure 3.2 illustrates the local magnetic field (H) distribution for both resonant conditions and clearly shows both GMR and SPR effects in play.

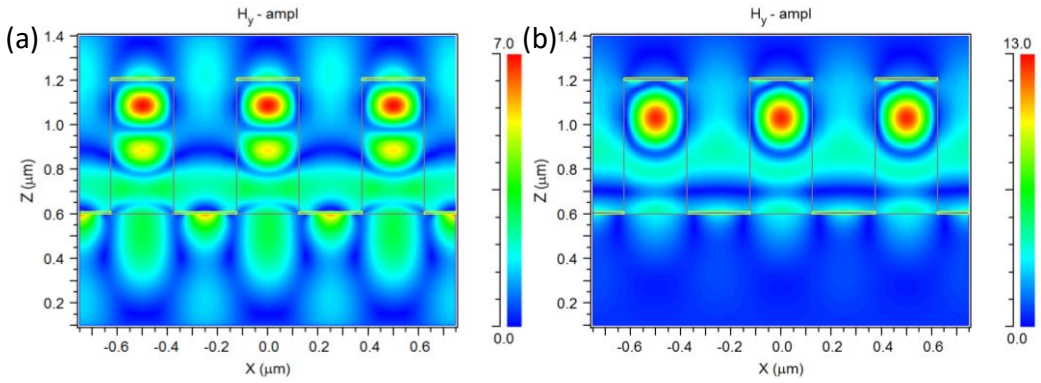

Fig 3.2 - (a) Magnetic-field distribution of the resonance at 785 nm for the gold-coated structure in Fig. 3.1(d) under TM polarized illumination. The local field signature implies a TM_1 mode with simultaneous SPR signature. (b) Same as (a) at 912 nm. The TM_0 mode is simultaneously excited with a SPR. Three grating periods are shown.

3.3 Experimental verification

Next, we present the design of photonic absorbers based on practical nanoimprinted resonance structures. These designs have been verified experimentally using etched silicon molds to imprint surface-relief gratings into polymers. The imprints are sputtered with a ~100 nm titanium dioxide film. A systematic study was then carried out to examine the effect of varying the thickness of the Au films sputtered onto devices described above.

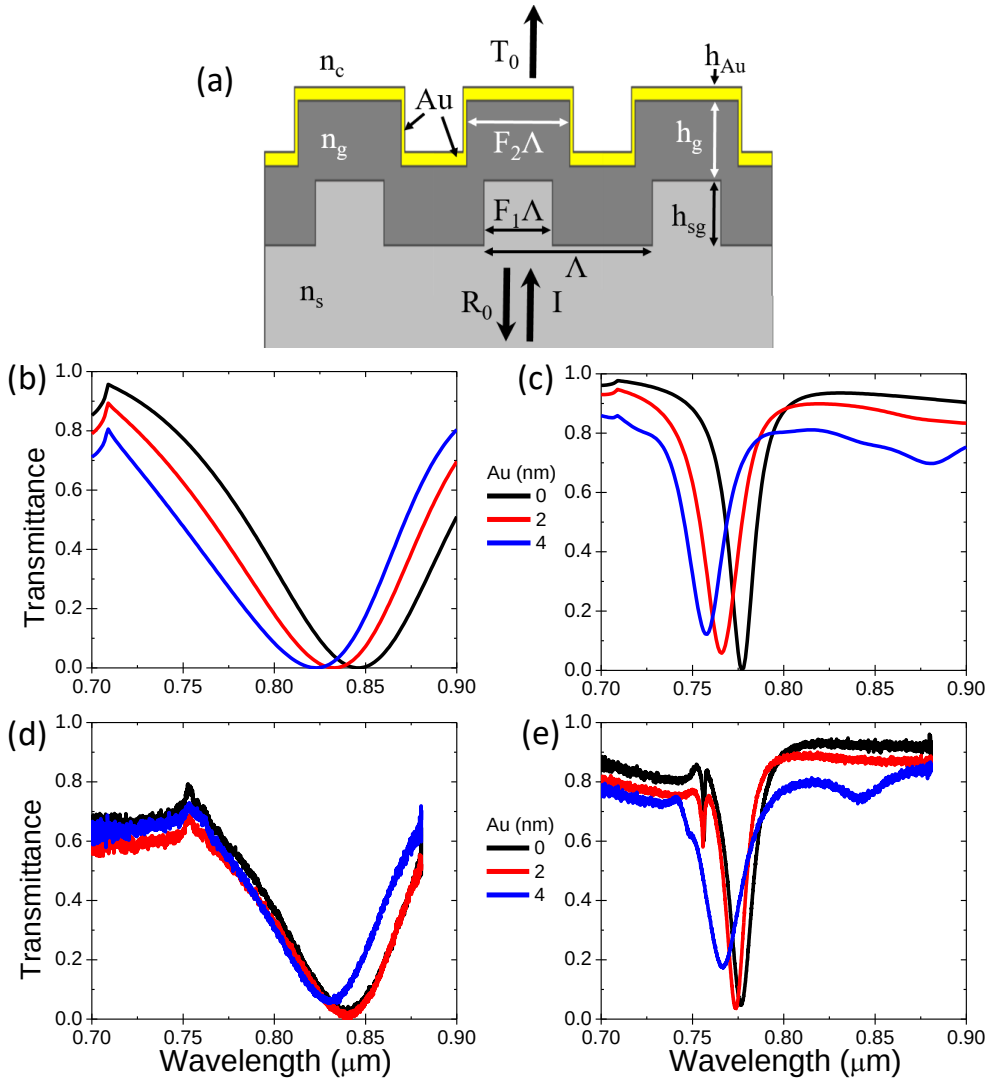

Fig. 3.3 - (a) Model of the fabricated devices where Λ = 460 nm, F_1 = 0.4, F_2 = 0.6, h_{sg} = 94 nm, h_g = 116 nm, n_s = 1.54, and n_c = 1. Simulation data for varying Au thickness for (b) TE polarized light; (c) TM polarized light. Experimental data characterized by the Au thickness for (d) TE polarized light (e) TM polarized light. 880 nm is the longest detectable wavelength for the optical spectrum analyzer (OSA) used.

Figure 3.3 illustrates the device structure and shows good agreement between the simulated and experimental response of devices with varying Au gold

top layer thicknesses. Results are presented for both TE and TM polarization using samples illuminated by polarized light at normal incidence in air. Atomic force microscopy (AFM), scanning-electron microscopy (SEM), and profilometry were used to measure the Au thickness on each device. It is worth noting that the Au layer is imperfect and may contribute to some discrepancies in the data. The GMR resonance wavelengths for the experimental devices match theory for both polarization states which is an important observation since these devices are sensitive to the angle of incidence and thus the spectra can be affected by imperfect collimation which accounts for some of the discrepancy.

The simulation results for the 4 nm Au coated device under TM polarized light at normal incidence are shown in Fig. 3.4. Two points of interest 758 nm and 880 nm are marked on the graph and the associated field distributions were simulated. The 758 nm resonance is strongly related to the GMR at 777 nm for the uncoated device. Meanwhile, the addition of the gold layer enables a SPR to form within the same band appearing at 880 nm in simulation but at a shorter wavelength in experiment. There is good agreement between theory and experiment as shown in Fig. 3.4(b) with corresponding H-fields plotted in Fig. 3.4(c,d). The plasmonic field pattern on the gold film on the top of the grating

ridge is a localized SPR resonance caused by the sharp spatial delimits of the Au strip.

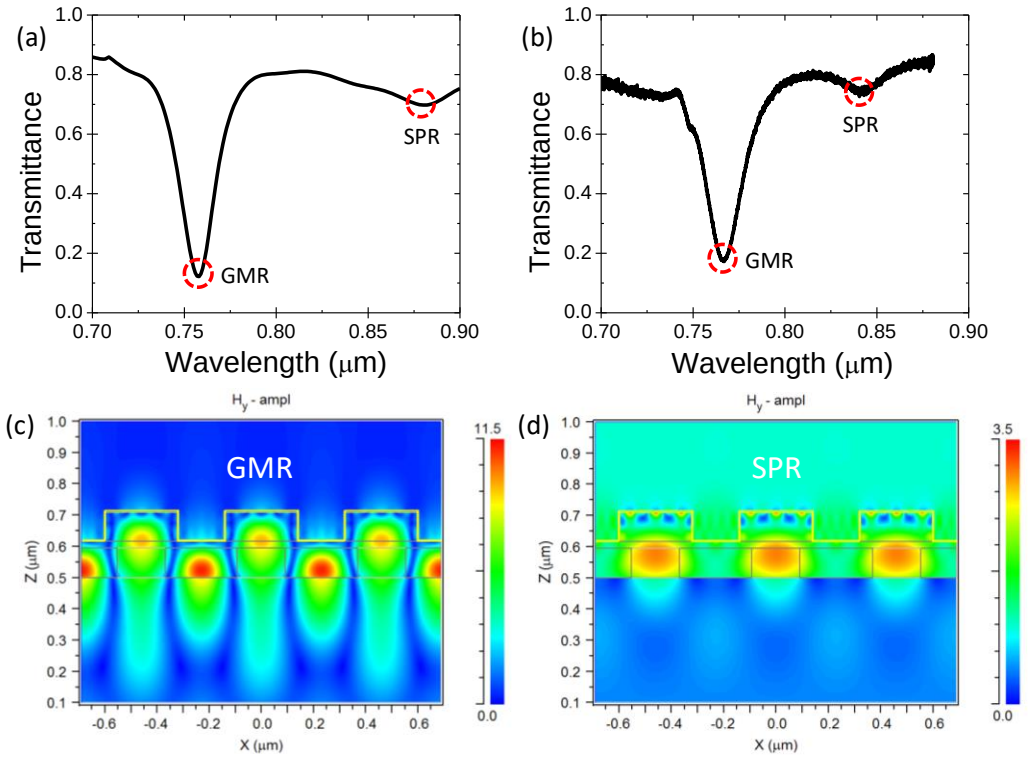

Fig. 3.4 - (a) Simulated performance of the 4 nm thick Au coated device. (b) Experimental measurement of equivalent device from (a). (c) Simulated energy distribution for the TM GMR at 758 nm from (a). (d) Simulated energy distribution for the TM SPR at 880 nm from (a).

Figures 3.5 (a-c) illustrate transmission, reflection, and absorption for the same basic device structure with varying gold thickness. The GMR response is quenched for increasing Au thickness and additional SPR modes can be created and manipulated through choice of Au thickness. Examples of representative H-

field distributions are shown in Figs. 3.5 (d-h). Wavelength dependence is exhibited by the spectral response as expected and these responses are either pure plasmonic modes or mixed plasmonic/GMR modes. Figures 3.5 (f) and (g) show a stronger GMR modal contribution compared to the (e) and (h) since the wavelengths in these cases are close to the original GMR wavelength of the unmetallized device. Transmission is completely suppressed in thick Au coatings with thickness>100 nm and only a strong SPR mode with nearly 100% absorption appears at 903 nm as seen in Fig. 3.5 (d).

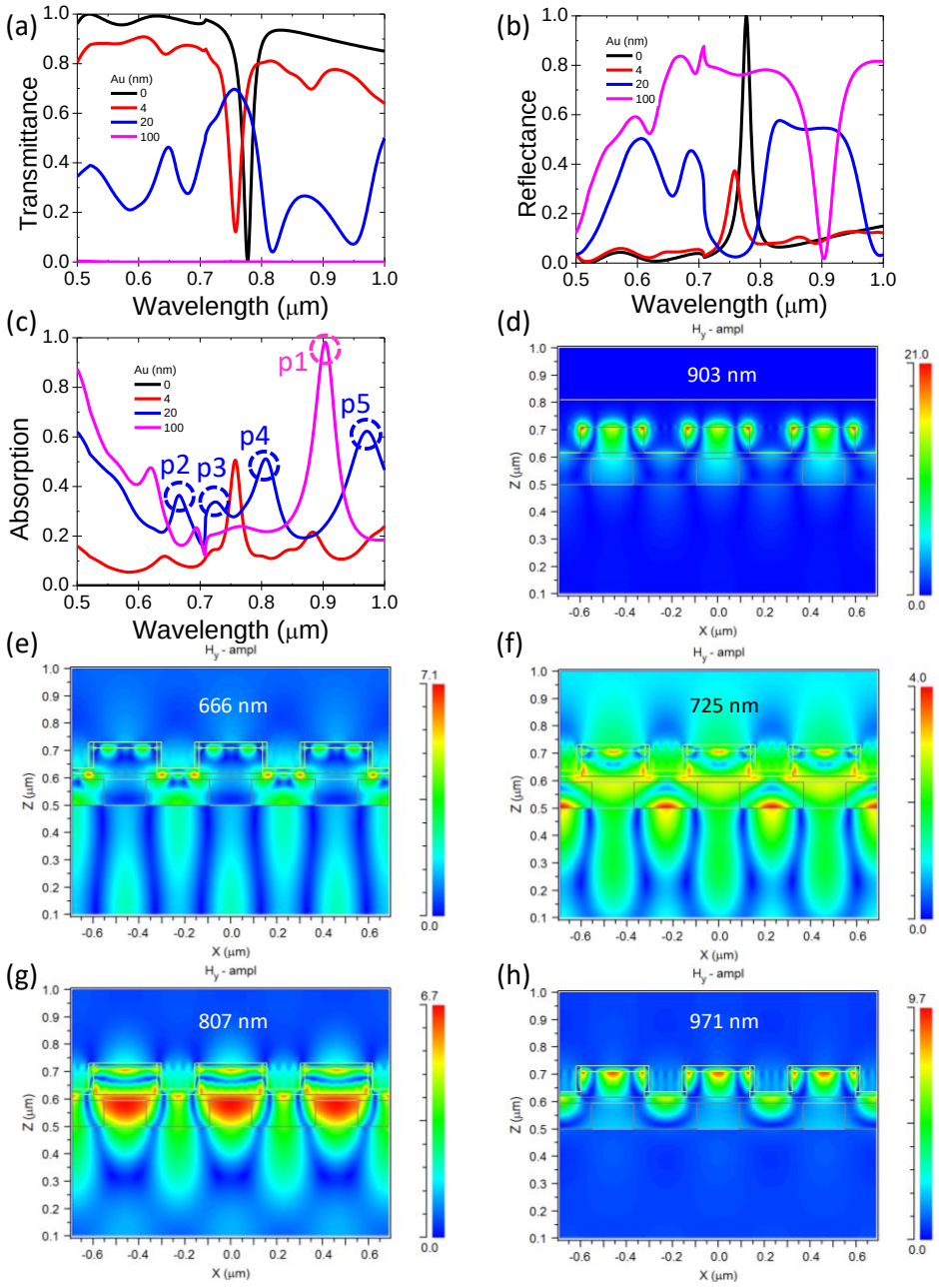

Fig. 3.5 - Simulation results for the nanoimprinted device structure in Fig. 3.3(a) for variable Au thickness (h_{Au}) under normally incident TM-polarized light with spectra for (a) Transmittance, (b) Reflectance, (c) Absorption. (d) Local H-field distribution for peak labeled p1 for the 100 nm Au film. (e) Field distribution for p2 for h_{Au} = 20 nm. (f) Field distribution for p3 for h_{Au} = 20 nm. (g) Field distribution for p4 for h_{Au} = 20 nm. (h) Field distribution for p5 for h_{Au} = 20 nm.

3.4 Hybrid sensors

GMR and SPR devices find many applications including imaging, detection and biosensing. Sensing is based on the of change in resonant wavelength (nm/RIU) or angle (degrees/RIU) compared to the change in the refractive index. Originally, Magnusson and Wang [6,7] suggested use of the GMR effect for sensor applications and disclosed GMR filters that could be tuned by changing resonance structure parameters including thickness and refractive index [32]. Tibuleac et al. [33] and Wawro et al. [9] presented new GMR biosensor designs with new applications of these sensors integrated with optical fibers. Kikuta et al. [10], Cunningham et al. [34,35], and Fang et al. [36,37] also discussed the use of these very same resonant elements as biosensors. The multiparametric capability of this sensor class based on polarization and modal diversity was subsequently described by Magnusson et al. in 2011 [11]. Hybrid modal/plasmonic sensors are only beginning to be studied. Magnusson et al. presented initial data that demonstrated this sensor concept and multiparametric detection possibilities [29]. Recently, Mizutani et al. showed high sensitivity for a dielectric grating deposited on a metal substrate [38]. This configuration enabled the use of a grating/guiding layer with a lower refractive index than the substrate.

Here we treat a mixed metal/dielectric sensor operating near the Rayleigh wavelengths for both substrate and cover media. Practical biosensing platforms often apply a substrate light entry and interrogate the sensor at normal incidence. This prevents the signal from passing through the analyte which may reduce the accuracy of the reading; we apply this operational mode. The proposed device has operational wavelength ~750-900 nm and is composed of SiO_2 and Al. To reduce attenuation of the signal passing through the sensor, the aluminum film is noncontiguous as shown in Fig. 3.6(a). The proposed device is atypical in that the grating/guiding material is the same as the substrate.

At normal incidence, the Rayleigh wavelength is given by $\lambda_R = n\Lambda$ where Λ is the period of the grating and n is the refractive index of the cover or substrate media. Obviously, the change of the index of refraction determined by the Rayleigh shift is $S = d\lambda_R/dn = \Lambda$ in nm/RIU. For the device in Fig. 3.6(a) and with a cover index of $n_c = 1.33$ we find the Rayleigh wavelength for the cover (λ_{RC}) to be 798 nm whereas the Rayleigh wavelength of the substrate (λ_{RS}) is 871 nm in agreement with the numerical results in Fig. 3.6. There, a GMR arises near λ_{RC} for TE polarized light at 799.3 nm as detailed in Fig. 3.6(b). It exhibits a classic Fano resonance shape with a peak and a dip.

The GMR sensitivity to the change in the cover index is to 530 nm/RIU for TE polarized light. The peak diminishes as the cover refractive index n_c increases. This is due to the proximity of λ_{RC} which, at a fixed Λ = 600 nm, has S = 600 nm/RIU. Therefore, λ_{RC} is more sensitive than the GMR peak wavelength and shifts more aggressively with variation of the cover index. Since a strong GMR typically exists in the subwavelength domain, we see the GMR peak diminish after λ_{RC} surpasses it at about n_c = 1.36. This progression is illustrated in Fig. 3.6(c). Figure 3.6(d) shows the lateral standing wave and field localization in the grating corresponding to the GMR dip in the spectra.

Strong Rayleigh anomaly signatures also appear for this device for TM polarized light. Although a GMR peak can be realized for TM polarization, for example at n_c = 1, the device parameters were chosen such that λ_{RC} has already surpassed the GMR thus eliminating it. Therefore, the sensitivity is S = 600 nm/RIU which is confirmed by λ_{RC} shift in Fig. 3.6(e). An absorption peak appears in the spectrum at ~λ = 822 nm for n_c = 1.33. The internal fields show plasmonic localization on the Al patches at that wavelength in Fig. 3.6(f).

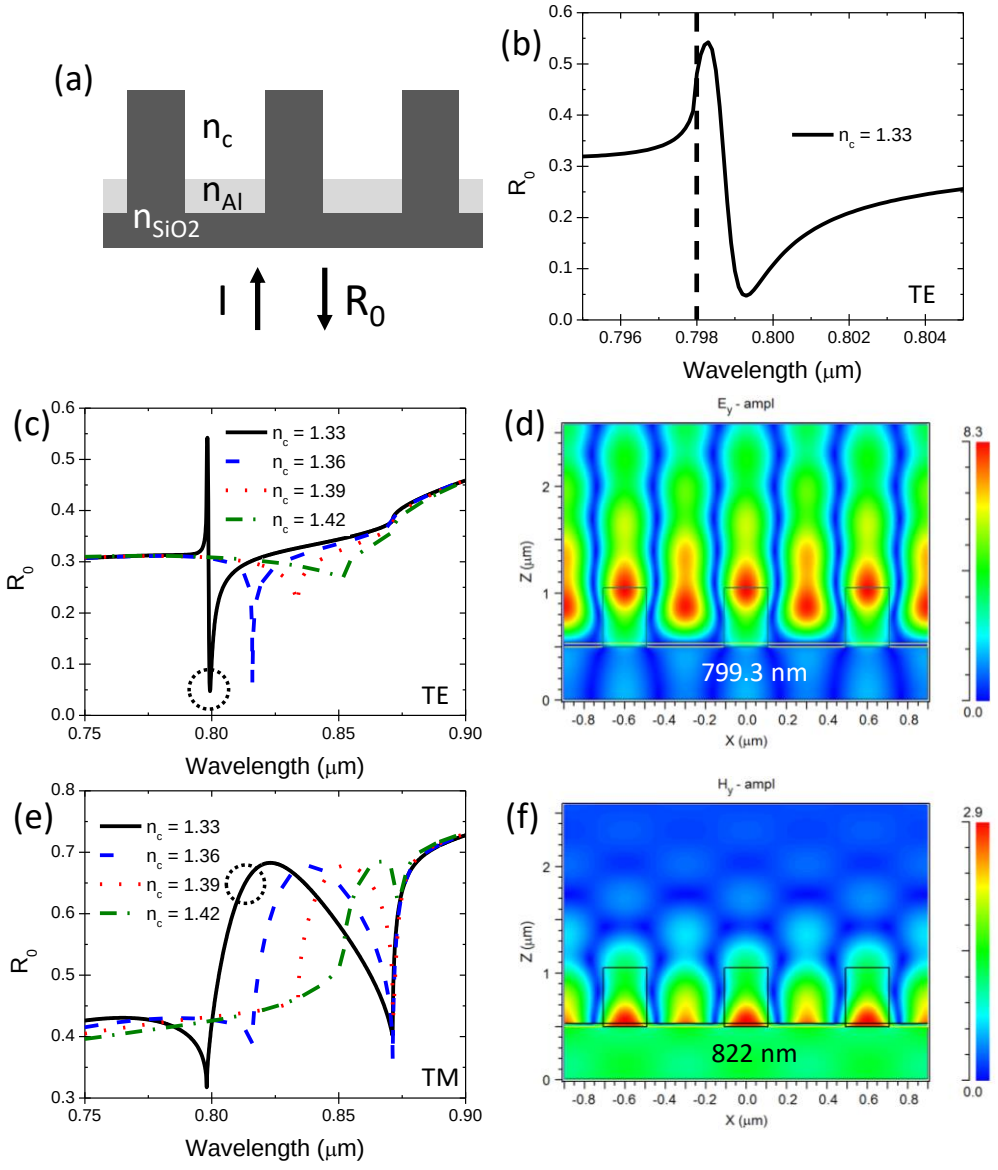

Fig. 3.6 - (a) Device model for the hybrid sensor. Λ = 600 nm, d_g = 550 nm, F = 0.36, d_m = 30 nm. (b) Detailed look of the TE response for n_c = 1.33. The dotted line represents the Rayleigh wavelength at 798 nm. (c) TE response for a shifting cover refractive index. A GMR peak can be seen to be overtaken by the Rayleigh anomaly. The circle represents a GMR peak at 799.3 nm for n_c = 1.33. (d) Field plot at the GMR wavelength from (c). (e) TM response for a shifting cover index. The Rayleigh anomaly has already overtaken the GMR peak. (f) Field plot of the circled wavelength from part (e) at 822 nm. SPR activity can be seen.

In both cases, in Fig. 3.6(e) for TE and TM polarized light, the Rayleigh wavelength for SiO_2 can be seen at 871 nm and does not exhibit any shift. Since the refractive index of the SiO_2 remains constant, this is to be expected. Therefore, the Rayleigh spectral dip at 871 nm is locked and can be used as a self-reference.

3.5 Hybrid display elements

As a final example, we consider the use of the hybrid elements under study in display technology. Color filters operating in transmission find use in imaging, computer monitors, and projection display systems. Color filters based on photonic nanostructures have advantages over dye-based filters such as tunability, compactness, and stability. Color filters are realizable with metal gratings [39], Fabry-Pérot resonators [40], and guided-mode resonant subwavelength gratings [41,42]. Good filtering performance has been shown with metallic gratings and two dielectric layers for waveguide and buffer cladding [43-46]. Our research group recently proposed a simple architecture with one metal grating and a single waveguide film [22].

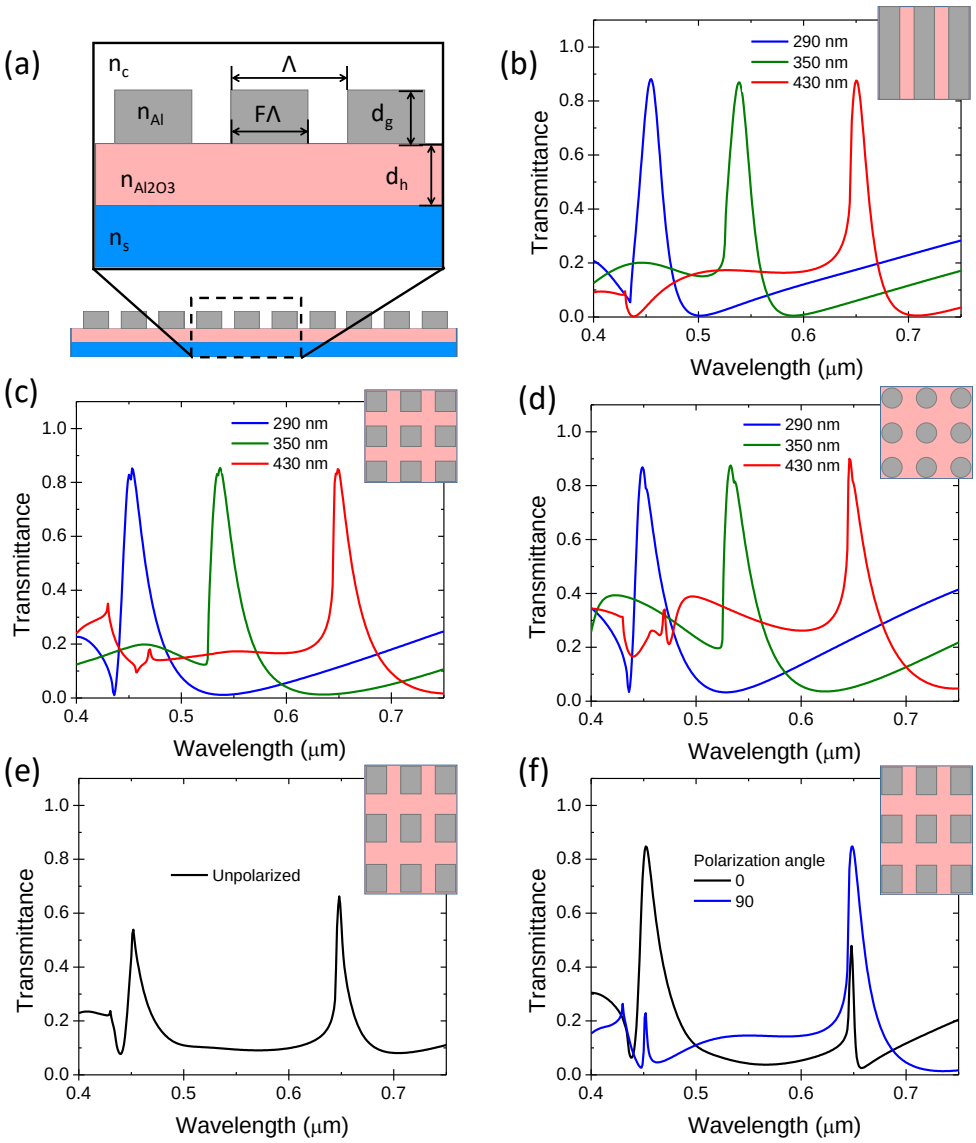

Fig. 3.7 - (a) Cross section of an Al-Al_2O_3 color pixel with critical dimensions. The period Λ is varied from 290 nm to 430 nm depending on the desired pass band. F = 0.67, d_h = 200 nm, d_g = 40 nm, n_c = 1, and n_s = 1.5. Each result is accompanied by a top view of the device. (b) TM polarized spectra of a model 1D device with varying periodicity. (c) Spectra of a 2D color pixel. (d) Spectra of a 2D color pixel utilizing circular rods in place of squares. (e) Spectra of a 2D color pixel utilizing two different periodicities. 290 nm is used for one periodicity whilst 430 nm is for the other. (f) Same device from (e) with different polarization angles.

The filter operates under hybridized guided-mode and surface-plasmon resonance effects near the Rayleigh anomaly wavelength. The experimentally demonstrated efficiency exceeded 80% and good color purity was obtained with narrow bandwidths of ~20 nm for three fundamental colors at λ = 454 nm, 536 nm, and 651 nm [22]. Here we develop analogous devices that are polarization independent via 2D nanopatterning.

Figure 3.7(a) illustrates a cross section of the canonical 1D device model. The spectral response for normally incident TM-polarized light is shown Fig. 3.7(b). Figure 3.7(c) shows the spectra for a corresponding 2D pixel where the 1D fill factor (F) is used in both grating directions. The characteristics of the 1D and 2D pixels are qualitatively similar. Due to symmetry, the 2D pixel is polarization insensitive at normal incidence. In fabrication with interference lithography, circular, rather than square, holes/posts appear naturally. Figure 3.7(d) shows the spectra pertaining to 2D circular post gratings.

Color mixing is possible with these devices by altering the periodicity along lateral orthogonal directions. Here we illustrate red and blue peaks by using periods of 290 nm and 430 nm along orthogonal directions as shown in the inset. Figure 3.7(e) shows that unpolarized light excites both resonances yielding a purple output but with lower efficiency than the previous 1D or 2D devices. Each peak can be selectively tuned by altering the input polarization as in Fig. 3.7(f).

Utilizing polarized light enables the device to select one of the dominant peaks with efficiency approaching that of the original device. Therefore, this would enable two filters to occupy the same space reducing the overall footprint with polarization-based output color selection.

3.6 Conclusions

In conclusion, we have investigated the properties of hybridized metal-dielectric elements for applications in optical engineering and photonics technology. We demonstrate that a simple grating with a thin gold film can be used excite hybridized GMR-SPR modes. We experimentally verify theoretical predictions with a surface-relief type GMR device sputtered with gold with various thicknesses. We then compute spectra and internal fields for the devices. The Au layer thickness controls the absorption spectrum with moderate thicknesses equalizing the absorption across the 500-1000 nm band. A thick coating of gold atop the grating generates nearly perfect absorption in a narrow band under pure SPR. Thinner coats are found to support hybridized GMR-SPR modes.

Furthermore, we introduce an interesting GMR/SPR sensor consisting of a thin subwavelength aluminum film integrated with a silicon-dioxide grating. The operational wavelength of the device lies between the Rayleigh wavelengths of the cover and the substrate. A GMR is excited by TE-polarized light and is

subsequently attenuated by the Rayleigh anomaly as the cover index increases. Moreover, under TM-polarized light, the device operates as a Rayleigh sensor. The Rayleigh wavelength corresponding to the substrate can be used as a self-reference. The sensitivity of the Rayleigh shift is simply S = Λ nm / RIU.

Lastly, we show the application of such devices to color filters. The 1D hybridized color filter operates under TM polarized light only while the 2D design allows polarization insensitivity for light at normal incidence. With dual distinct periods along orthogonal directions, two resonant peaks are induced within the visible spectrum for unpolarized light thus implying a color-mixing effect. The output color of the dual pixel is tunable with the input polarization state.

Chapter 4

Techniques for designing highly absorbing thin-film silicon structures utilizing guided-mode resonance, Rayleigh anomaly, and 2D expansion

4.1 Introduction

Absorption is a fundamental and often a desirable trait exploited for use in multiple applications including photodetectors and solar cells. The visible region, assumed here to range from 400 nm to 700 nm, is of particular interest in the field of solar cells. Efficient and cost effective means of harvesting additional light in this bandwidth has been a topic for many years with many solutions proposed [1-3]. In practice, solar cells produced today are often enhanced via random patterning at the surface to scatter light laterally into the active region effectively elongating the optical path length and thus enhancing absorption [1-4]. Highly periodic grating structures in both 1D and 2D topologies have been suggested in place of random surfaces to accomplish the same goal [1-7]. Such concepts are generally not pursued in industry due to the relative cost restraints inherent in fabricating such structured devices. If the additional costs are to be justified, a design would have to incorporate several key features. Namely, the design would

have to significantly enhance absorption across the visible region for incoherent light, be cheap to fabricate, and use photoactive materials like hydrogenated amorphous silicon (a:Si-H). Here, we apply principles of GMR [8-11] to enhance a thin film of a:Si-H with a total thickness akin to what is used in industry today.

The Rayleigh anomaly dates back to more than a century ago when Rayleigh offered the first explanation for Wood's anomalies in periodic surfaces in 1907 [12]. In practice, the Rayleigh anomaly, or Rayleigh wavelength (λ_R), manifests itself as a sharp feature in the spectrum marking a transition whereby high order diffraction becomes impossible at longer wavelengths. The phenomena has been used to shape the response of several devices [8,13]. In this chapter, we take advantage of two Rayleigh anomaly wavelengths. Namely, we use the Rayleigh wavelengths of the cover (λ_{RC}) and the substrate (λ_{RS}) to help shape the response of the device.

Both GMR and the Rayleigh anomaly exist for one dimensional (1D) and 2D gratings. For the most part, the physics for both 1D and 2D resonance phenomena remain the same. Specifically, the Rayleigh anomaly, which is dependent on periodicity, remains at the same spectral location for a 2D design of identical period. Similarly, GMR peaks can be realized through the same leaky-mode excitation as in the 1D case, albeit with a more complicated relationship relating

the grating to the guiding structure. In previous work it has been shown that direct conversion of a polarized 1D GMR device to 2D can yield a similar unpolarized response [14].

In summary, we present a theoretical structure suitable for use as a wideband absorber with special attention given to solar cell applications. We arrive at our design after applying a logical and straightforward optimization approach to a previously reported device to further enhance its capabilities. Our approach takes advantage of several well-known concepts including guided-mode resonance (GMR), Rayleigh anomaly, and 2D expansion. The device is shown to be insensitive to polarization and angular incidence. The structure is compared to a planar equivalent and shown to outperform it. At normal incidence, we report a polarization insensitive device capable of absorbing upwards of 80% of all visible light with a ~110 nm band achieving higher than 97% absorption.

4.2 Design and simulation

A 1D zero-contrast GMR device is composed of a substrate, often glass, a guiding material, and a cover. The guiding material will be patterned such that a grating is etched partway leaving a homogenous layer of the same material

adjacent the grating. The critical parameters of such a design include the periodicity (Λ), homogenous layer height (d_h), grating height (d_g), and the grating fill factor (F). Figure 4.1 illustrates a typical 1D zero contrast GMR.

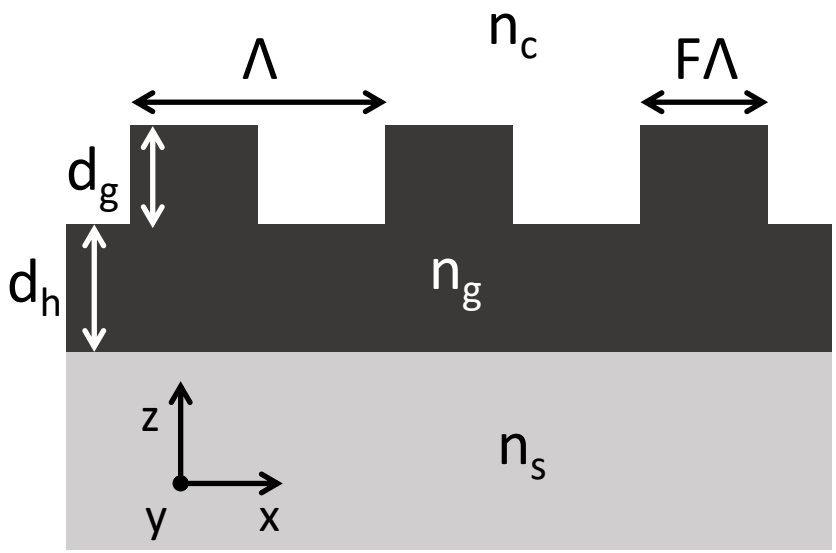

Fig. 4.1 - Depiction of a zero-contrast GMR structure with critical dimensions marked. The different materials used are denoted by differing refractive indices of the cover (n_c), the guiding material (n_g), and the substrate (n_s).

Years ago, our group wrote a letter detailing a 1D a-Si:H GMR design atop SiO_2 offering high absorption across the visible region [6]. That particular design was optimized for nearly perfect absorption (>98%) across a 100 nm spectral band near the middle of the visible region, where sunlight at the Earth's surface has the most energy, for TM polarized light. While the TE polarized light benefited from a

moderate boost in absorption over its planar counterpart, it was far from perfect, generally remaining close to 60% across the visible region. The design loosely took advantage of λ_{RS} to avoid losing diffracted transmission energy into the substrate. While λ_{RC} was visible in the predicted results, it was not explicitly used to shape the response. In this chapter we have chosen to start with our previous design mentioned above and expand upon it using the aforementioned techniques and phenomena.

To start, we have derived a dispersion curve for a-Si:H using several sources including in-house ellipsometry measurements [15,16]. The resulting curve is displayed in Fig. 4.2. It is worth noting that sputtered a-Si yields a slightly higher absorption, particularly at longer wavelengths. This implies that higher absorption within the same design is possible if the application is not reliant upon the electrical properties.

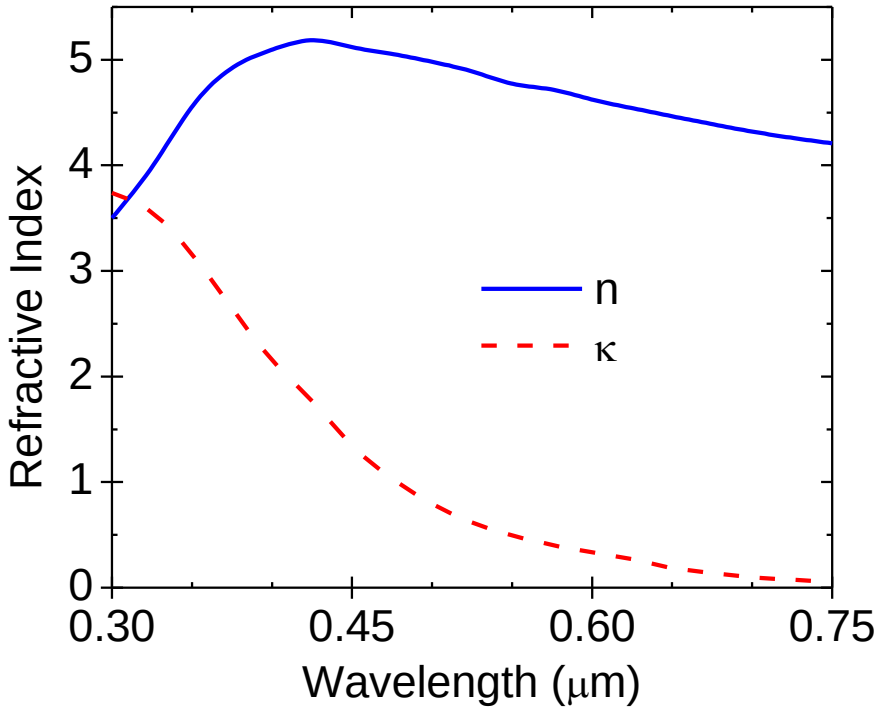

Fig. 4.2 - Dispersion curves for a-Si:H used in this chapter.

The first step in enhancing the design involves converting the structure into 2D. A direct recreation of the device in 2D would have the same periodicity and fill factor in both lateral directions. This results in a square grating atop a homogenous layer. From an economic perspective, laser interference lithography (LIL) offers versatility for creating gratings as the periodicity and fill factor can be altered without the use of traditional masks. Furthermore, LIL can be scaled for

use across large areas unlike techniques such as e-beam lithography (EBL) [17]. If we are to assume LIL as the means of fabrication, square gratings pose a problem as 2D LIL masks create elliptical profiles. If instead we assume an elliptical grating with identical diameters in both lateral directions we arrive at a cylindrical grating structure. Provided we wish to keep all of the parameters the same in the lateral directions, our original critical dimension F now changes to diameter (D) where it should be written as a fraction of Λ. The resulting device will have similar a GMR response to that of its 1D counterpart and will have Rayleigh anomalies at exactly the same places.

The second step in optimizing the design is to alter where the Rayleigh anomalies arise to help shape the response. For this design, we generally find that transmission is quite low while reflection can often account for the majority of the energy. Therefore, our primary concern is with controlling reflected diffraction. Assuming normal incidence, λ_R is given as $\lambda_R = n\Lambda$ where n is the refractive index of the material in question. If we assume the device will operate with an air cover ($n_{air} = 1$) then $\lambda_{RC} = \Lambda$. Provided we are interested in maximizing the absorption between 400 nm and 700 nm it makes the most sense to assign $\Lambda = 400$ nm. This way there are no high order reflections that are emitted from the device. Fortunately, with $\Lambda = 400$ nm and a substrate index (n_s) of ~1.48 we find that λ_{RS}

~ 592 nm, near the middle of our band. This proves to be useful in propping the absorption band up further lending that a periodicity of 400 nm is appropriate for the design. Furthermore, at wavelengths longer than 592 nm we can take advantage of GMR conditions to further prop up the absorption curve.

After assigning the period, we have reduced the parameter set to three. Namely, d_h, d_g, and D. If we assume we want a design between 300 nm and 600 nm thick, a desirable thickness in industry [18], and limit D to between 0.3 and 0.7 for fabrication concerns, we can use forward methods for honing our design. Utilizing rigorous coupled wave analysis (RCWA) we run several sweeps to optimize our parameter set and arrive at Λ = 400 nm, d_h = 350 nm, d_g = 120 nm, and D = 0.64. Figure 4.3 illustrates a conceptual model and our results assuming unpolarized, normally incident light.

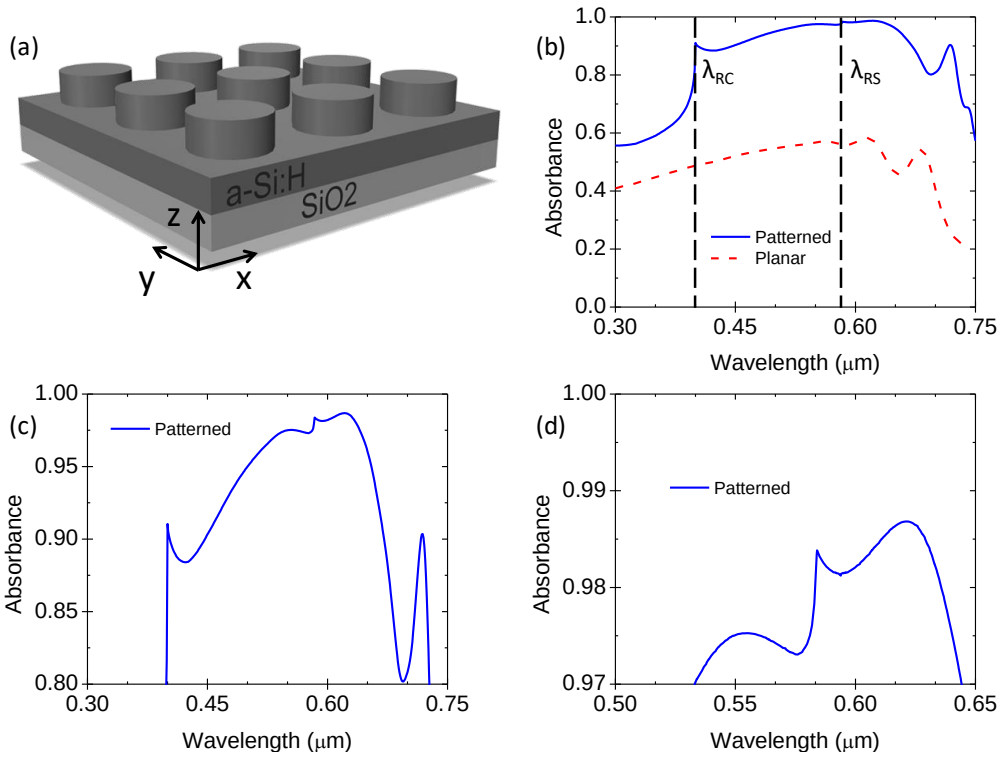

Fig. 4.3 - (a) Conceptual design of 2D device. (b) Theoretical performance of wideband absorber after optimization, Rayleigh wavelengths are marked by dotted lines for the cover and substrate. (c) Zoom in of results indicating absorption across the visible band. (d) Zoom in of results indicating nearly perfect absorption across ~110 nm.

As shown in Fig. 4.3, the design functions well for unpolarized light at normal incidence. The entire visible region enjoys an absorption upwards of 80%. Furthermore, there is a region near the center of the band with a bandwidth of ~110 nm that experiences upwards of 97% absorption. The Rayleigh wavelengths are clearly shown and have a positive effect on shaping the absorption curve.

Typically, a solar cell is aimed as directly towards the sun as possible. Even still, it is unrealistic to only assume normal incidence on the device. Here we present a study comparing the angular sensitivity of our device compared to a planar cell of the same thickness. It is assumed that the angle is varied in a single plane orthogonal to the interface but aligned with one of the lateral directions. Figure 4.4 illustrates our results.

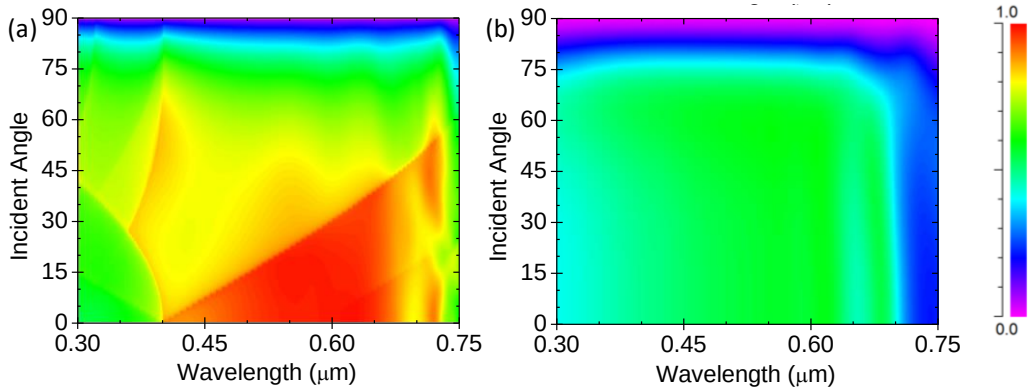

Fig. 4.4 - Performance comparison between the optimized 2D design (a) and a planar surface (b) of the same thickness across all incident angles.

As shown in Fig. 4.4, our design is superior to the equivalent planar cell and continues to perform well even at large angles.

4.3 Discussion

The work presented indicates the strength and versatility of utilizing multiple phenomena in conjunction with each other. A relatively straight forward optimization process has yielded an effective means of enhancing absorption within an a-Si:H layer. The design offers polarization and angular insensitivity. In comparing a planar cell to the patterned one it is clear that the patterning offers significant advantages. To further illustrate this, we present a chart comparing the performance of the patterned and planar devices. Figure 4.5 illustrates the integrated and normalized absorbance across the visible region for both devices at varying angles along a plane orthogonal to the interface but along one of the lateral axes. The graph simultaneously illustrates the comparative advantage of the patterned cell over the planar by plotting the enhancement factor as a function of angle.

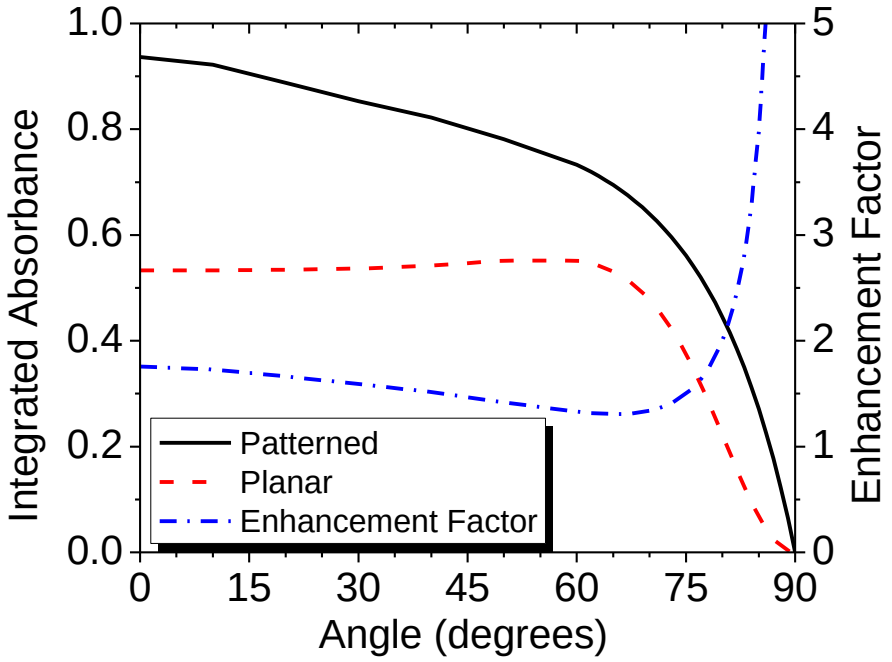

Fig. 4.5 - Integrated and normalized absorption curves across the visible region (400 – 700 nm) for the patterned and planar designs.

Figure 4.5 indicates that the patterned cell is more efficient than the planar one at every angle with the highest gains at the steepest angles. For typical operation as a solar cell, with angles at or near zero, we find the enhancement factor for the patterned device is ~1.75 times its planar counterpart.

4.4 Conclusions

We have presented techniques and discussion on how to optimize thin film absorbers. Starting with a simple design, we employ the use of Rayleigh anomaly, GMR, and 2D expansion to further optimize the design for wideband absorption. The resulting device is shown to achieve polarization independence whilst simultaneously locking in gains in absorption over its planar and 1D equivalents. The design boasts an absorptivity above 80% across the visible band with a ~110 nm band achieving nearly perfect absorption above 97%. The design is shown to outperform its planar equivalent at every angle.

Chapter 5

GMR assisted absorbing ultra-sparse grating polarizers

5.1 Introduction

Polarizers are fundamental components in optics with applications ranging from optical measurements and sensing [1-3] to coherent applications and display technology [1-4] amongst many others. They can derive their characteristics from selective absorption, resonance effects, birefringence, Brewster angle, plasmonics [5-10], and more [2,3]. The extinction ratio is the most common metric used to measure the capability of a polarizer and can range from about 10:1 to roughly 10^7:1 for commercially available devices. Common types of linear polarizers include wire grid polarizers (WGP) [3,11-13], polarizing beam splitters [3], birefringent crystals [3], and thin films [14-21]. Among these, thin films stand out as a versatile option which can be tailor made to suit specific purposes [19]. Within the field of thin film polarizers, sparse grating topologies stand out as an intriguing device class which yields useful properties despite remaining materially sparse [21]. Here, we aim to expand upon the potential for absorbing polarizers based on thin film sparse gratings.

Thin film gratings lend themselves to several types of phenomena including Rayleigh anomalies [6] and periodic resonances [6,19]. Among these, guided-mode resonance (GMR) is among the most interesting with demonstrated uses in filtering [19], sensing [20], and polarizing optics [19,21] amongst others [19,22]. Nearly lossless sparse GMR gratings have been previously demonstrated in the near IR [21]. Additionally, sparse antireflection polarizers absent GMR have also been discussed previously [17].

5.2 Design and simulation

Through rigorous coupled-wave analysis [23] (RCWA) we investigate a series of sparse, high aspect ratio gratings composed of silicon and note preferential absorption of TE polarized light and transmission of TM polarized light. Utilizing forward design techniques we arrive at a family of devices composed of amorphous silicon (a-Si) on SiO_2 lending itself for use in the near UV and the shorter end of visible where the absorption coefficient remains high. Figure 5.1 depicts the grating profile and the performance of a sample device consisting of a periodicity (Λ) of 280 nm, a fill factor (F) of 0.05 or 5%, and a grating height (d_g) equal to 100($F\Lambda$) implying an aspect ratio of 100. This is beyond the limits of current fabrication technology but serves well as a demonstration. It is found that

the conceptual device provides a low reflection, high extinction ratio polarizer where the TE reflectance is never in excess of 10% at the center wavelength of 481 nm.

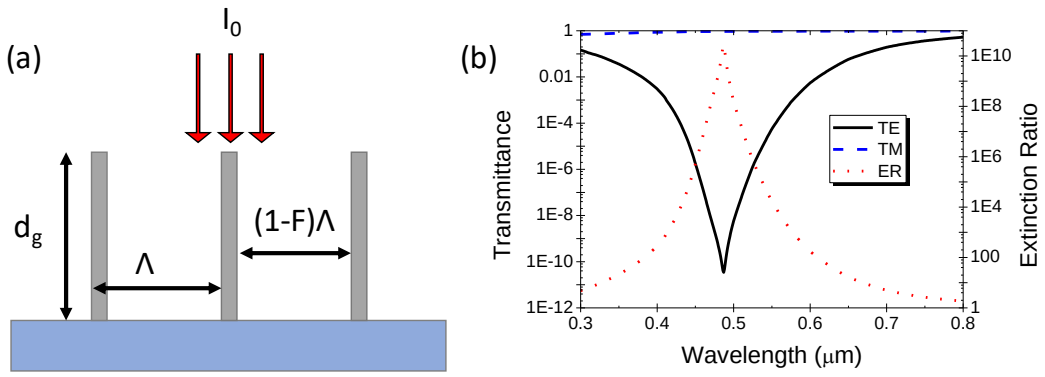

Fig. 5.1 - (a) Illustration of a sparse grating topology with critical dimensions marked. Performance of a theoretical device with Λ = 280 nm, F = 0.05, and d_g = 100(FΛ). Extinction ratio is shown on the right axis.

Designing such elements relies on combining several phenomena. We find that the most critical feature of such an element is the fill factor. In Fig. 5.2 we illustrate the effects of altering the fill factor for a grating with Λ = 280 nm and an aspect ratio of 100.

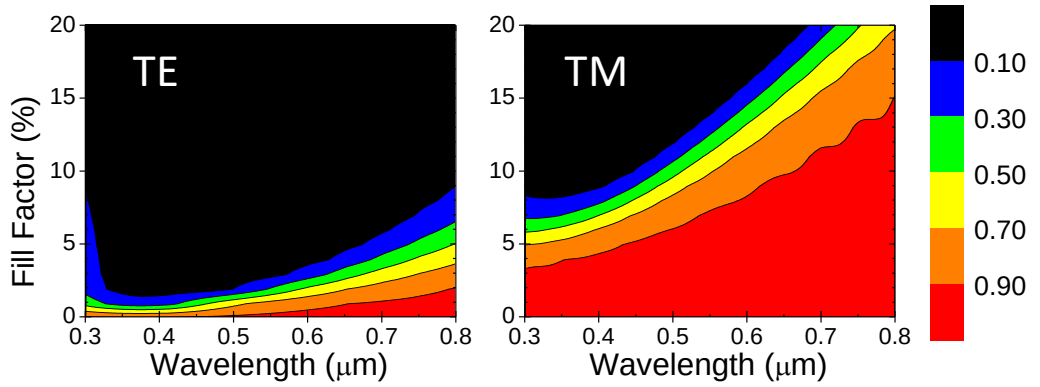

Fig. 5.2 - Transmittance for TE and TM polarized light for a varying fill factor (F) assuming Λ = 280 nm and $d_g = 100(\Lambda F)$.

From Fig. 5.2 one notes that the most suitable region for a high extinction ratio occurs for ultra sparse gratings, taken here to mean a fill factor of less than 10%. In this chapter, we will predominantly discuss devices with F = 0.05 or 5% which can be seen to have a large region in which the TE transmittance is low while the TM is allowed to pass with low attenuation. In order to understand why this occurs, it makes sense to observe the fields in the device. Figure 5.3 illustrates field plots for both TE and TM polarized light for a similar device to the one used in Fig. 5.1 (b) at the center wavelength 481 nm with the absorption coefficient artificially set to zero.

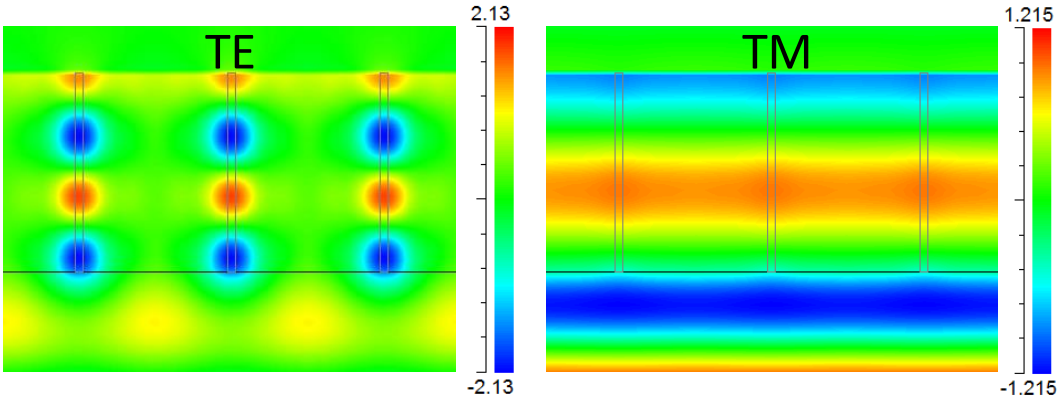

Fig. 5.3 - Field plots for both TE and TM polarized light in a lossless device with λ = 481 nm, Λ = 280 nm, F = 0.05, and an aspect ratio of 27. The simulation negates absorptive effects of the silicon to more effectively show the fields.

Figure 5.3 illustrates the predominant mechanism that enables the device to function. Namely, TE polarized incident light is found to undergo strong vertical coupling into the gratings whilst TM polarized light is able to pass through without strong coupling, thus avoiding exposure to the lossy silicon layer. This implies that a thicker grating will produce a higher extinction ratio provided that the TM polarized light continues to transmit without significant attenuation. This is a similar response to that seen in WGPs. In order to test this hypothesis, we investigate the effects of scaling the aspect ratio and its effect on the extinction ratio. Figure 5.4 illustrates those results compared to a similar WGP composed of aluminum on SiO_2.

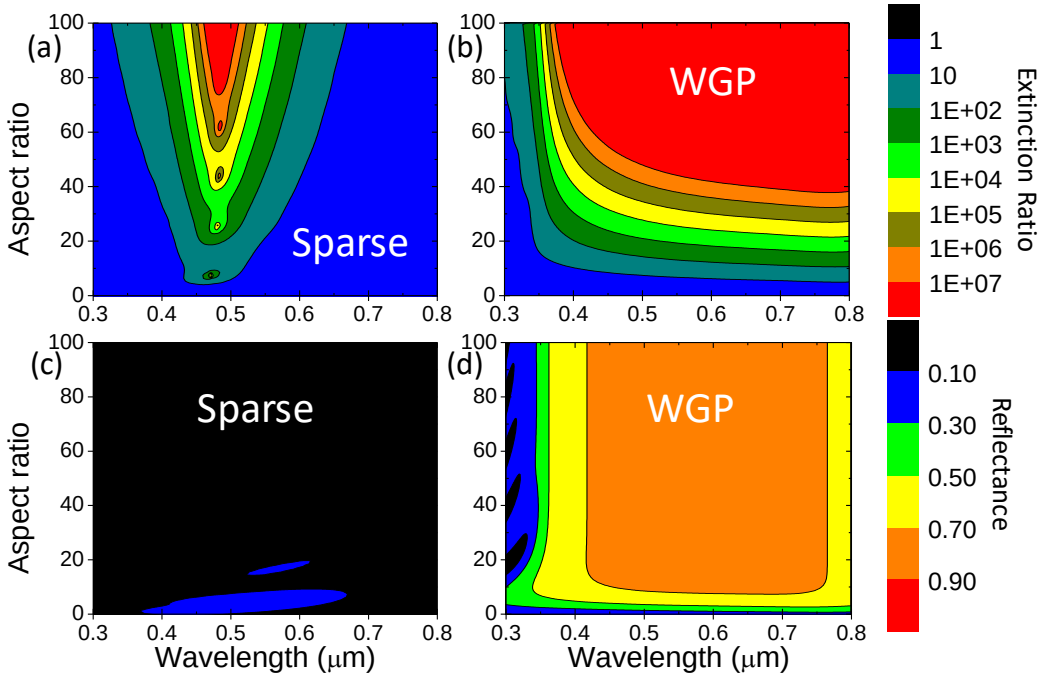

Fig. 5.4 - (a) Predicted extinction ratio (ER) as a function of aspect ratio and wavelength for a sparse grating with Λ = 280 nm and F = 0.05. (b) ER as a function of aspect ratio and wavelength for a WGP with Λ = 140 nm and F = 0.05. (c) Reflectance data for the rejected TE light for the same sparse grating. (d) Reflectance data for the rejected TE light for the same WGP.

The results from Fig. 5.4 (a) prove our hypothesis illustrating that, in general, a thicker grating will yield a higher extinction ratio. This trend continues well past the AR = 100 mark pushing the feasibility of the device outside the realm of current fabrication technology. In fact, we find that the device continues to improve even for aspect ratios in excess of 1000 whereby the extinction ratio can increase, in theory, upwards of 10^{19}:1, albeit with a TM transmittance of only ~10% at 350 nm. Wire grid polarizers can perform similarly as shown in Fig. 5.4 (b) and

even support wideband performance. However, wire grids will suffer from a similar attenuation and will predominantly reflect the rejected polarization as seen in Fig. 5.4 (d). Additionally, the periodicity for an equivalently operating wire grid polarizer is often much smaller than their dielectric counterparts, in this case half of the dielectric period. We have chosen to limit our investigation to AR ≤ 100 as it gives a broad view while remaining reasonably close to sizes reported in other devices [24,25], albeit with different structures and materials. Intriguingly, we observe some regions which experience an uncharacteristically high extinction ratio for the dielectric grating device that does not appear to follow the general pattern. These hot spots can be seen to occur in Fig. 5.4 (a) around $\lambda = 481$ nm for AR = 9, 27, 45, 63, 80, and 98. In order to explain these regions, additional analysis is needed.

The periodic subwavelength nature of these devices immediately lends suspicion towards resonant effects like GMR. In order to investigate whether or not GMR is responsible for these discontinuities we investigate several devices focusing on several of the discrete ratios listed above. By artificially changing the absorption coefficient of the silicon to zero we are able to see several characteristic GMR signatures in the response. However, the observed GMRs occur much earlier in the band than expected. Namely, the bulk of the resonances

occur before 440 nm, significantly shifted from the expected value of about 481 nm. In order to test whether or not these resonances can be attributed to the increased performance we have provided an additional study where the effects of restoring the absorption curve are investigated for a single device with a fixed aspect ratio of 27. Figure 5.5 illustrates these findings.

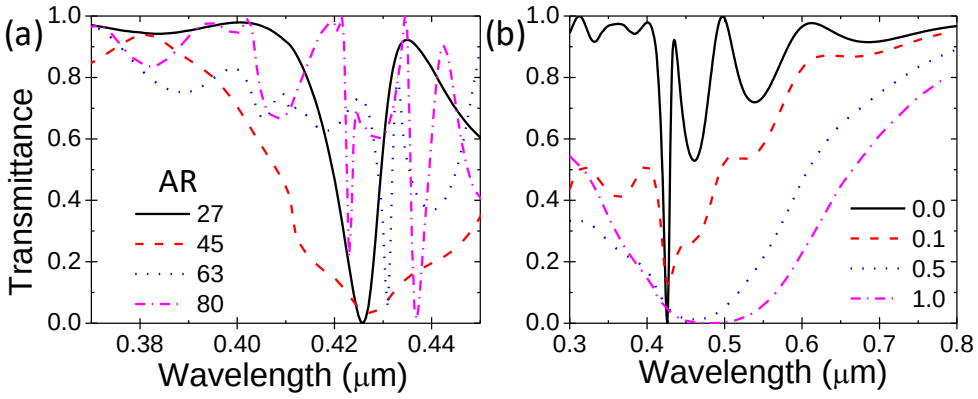

Fig. 5.5 - (a) Lossless response of several devices from Fig. 5.4 illustrating the presence of GMR. (b) Illustration of the effects of scaling the absorption coefficient revealing a forward shift in the minimum transmittance for a fixed aspect ratio of 27.

The results from Fig. 5.5 help to clarify several important nuances about the device. First, we note the presence of GMR as predicted previously. This implies, at a minimum, that the device is aided by the presence of GMR. Figure 5.5 (b) further lends support to our hypothesis as it clearly shows the transmittance minimum shift forward to the expected value of 481 nm as absorption is scaled between zero and one.

5.3 Discussion

As a final point of discussion, it is worth exploring the angular tolerance of these devices. It is found that the center wavelength has a high tolerance which decays the further away from the center wavelength the operation deviates. This is of particular use in laser applications where polarizing elements must minimize reflections back into the lasing cavity. Perhaps the easiest way to accomplish this goal is to avoid optics at normal such that the zero order reflection does not retrace its path into the cavity. Thus, a high tolerance in the operating angle is desirable. Figure 5.6 illustrates the resulting extinction ratio across the band for varying angle for the same device explored in Fig. 5.1.

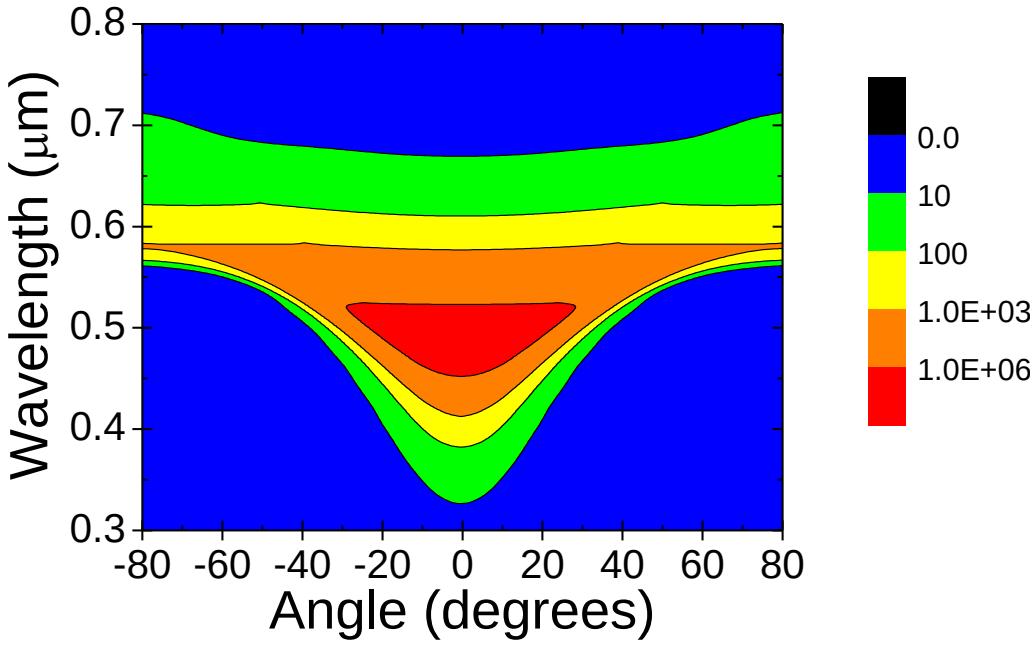

Fig. 5.6 – Angular tolerance of the same device from Fig. 5.1(b) with ER expressed as a color scale.

5.4 Conclusions

In conclusion, we have demonstrated a type of absorbing polarizer based on thin film, absorbing dielectric, sparse gratings. We find that TE polarized light is selectively absorbed via vertical coupling to the grating structure. Intuitively, a thicker grating leads to, in general, higher absorption of TE polarized light. When observing the extinction ratio as a function of aspect ratio, it becomes clear that certain hot spots exist for particular values. Through additional analysis we conclude the presence GMR conditions within the device. Specifically, the GMR

conditions appear at shorter wavelengths than expected where the absorption of the silicon material is higher. By slowly scaling absorption back into the simulation we are able to conclude a red shift in the minimum transmission wavelength for each of the observed resonances accounting for the discrepancy in the lossless resonant wavelength. In total, the device leverages multiple phenomena to create a theoretical absorbing polarizer with high extinction ratios.

Chapter 6

Mid IR GMR absorbers utilizing superlattice structures

6.1 Introduction

In recent years the need for new photodetectors in the mid IR, taken here to range from 8-12 μm, has been identified as technology approaches the theoretical limitations of mercury cadmium telluride (MCT) based detectors [1,2]. Amongst others, one promising technology comes in the form of the so-called type 2 super lattice (T2SL) [3]. While theoretically advantageous, T2SL topologies remain largely impractical due to low absorption coefficients directly translating into poor quantum efficiency (QE) [3]. Like many detectors, increasing the thickness of the device can increase the QE but reduces the signal-to-noise ratio [4].

In the past, there have been many proposals for enhancing absorption within a material [4-7]. The most common element in these proposals is to elongate the optical path length (OPL) via random or structured patterning. The use of patterned structures often gives rise to the use of such concepts as guided-mode resonance (GMR) and plasmonics. Previously, plasmonics have been cited as a possible method for enhancing absorption in T2SL structures [8]. While

appreciable gains in absorption can be made with this method, much of it is accounted for as ohmic losses which cannot be utilized by a typical detector. For instance, of the reported devices, two were nearly perfect absorbers. That said, each of the designs showed appreciable ohmic losses implying significant amounts of energy that could not be taken advantage of in the T2SL where it could be utilized in a detector. Here, we will illustrate appreciable gains in absorption for a T2SL structure utilizing GMR. This may represent an advantage as any gains in absorption within a GMR topology will be obtained within the material itself making it useable for detection.

As discussed above, GMR is achieved when an incident wave successfully couples to a periodic film. Historically, GMR structures have been studied most in the visible to near-IR spectral domains [9,10]. That said, the fundamental concepts that govern GMR are scalable and therefore applicable to concepts in the mid-IR and beyond.

As far as photodetectors go, Khaleque et al. demonstrated that GMR topologies can be applied to PiN diodes for solar cell applications [11]. While different in application, the operating principles behind the device prove the concept of integrating photodetection with GMR architectures.

6.2 Device modeling and structure

Here, we have chosen to use a T2SL model from Goldflam et al. [8]. To provide a fair comparison, we have opted to limit our device height to the same 1.77 μm used by Goldflam et al. who demonstrated a plasmonic array atop a T2SL structure to enhance the absorption. Utilizing numerical design methods, we arrive at a family of two-dimensional (2D) GMR structures with a periodicity (Λ) ranging 3-7 μm, a fill factor (F) ranging 0.3-0.8, and a total height whereby the homogenous layer height (d_h) and the grating height (d_g) are equal to 1.77 μm. For each of these designs, F is the same in both lateral directions.

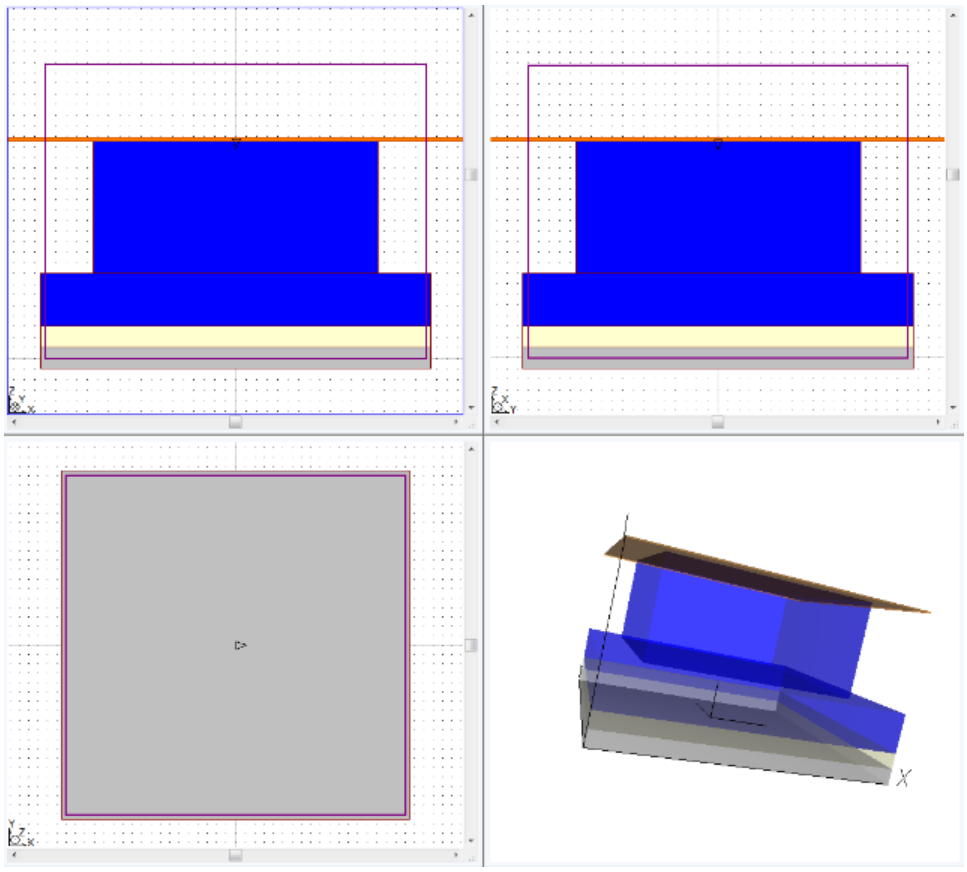

Fig. 6.1 – Sample device model for a T2SL GMR based absorber. F in both lateral directions is the same.

The use of a 2D structure eliminates the polarization sensitivity inherent to GMR devices. In addition, the cover and the substrate have both been chosen to be lossless in the simulation. By limiting our structure design to lossless materials besides the T2SL we can conclude any and all observed absorptive losses are caused by the active material alone. Figure 6.2 illustrates several curves for a device consisting of F = 0.75, d_h = 0.5 µm, d_g = 1.27 µm, and 3.5 µm $\leq \Lambda \leq$ 5.5 µm.

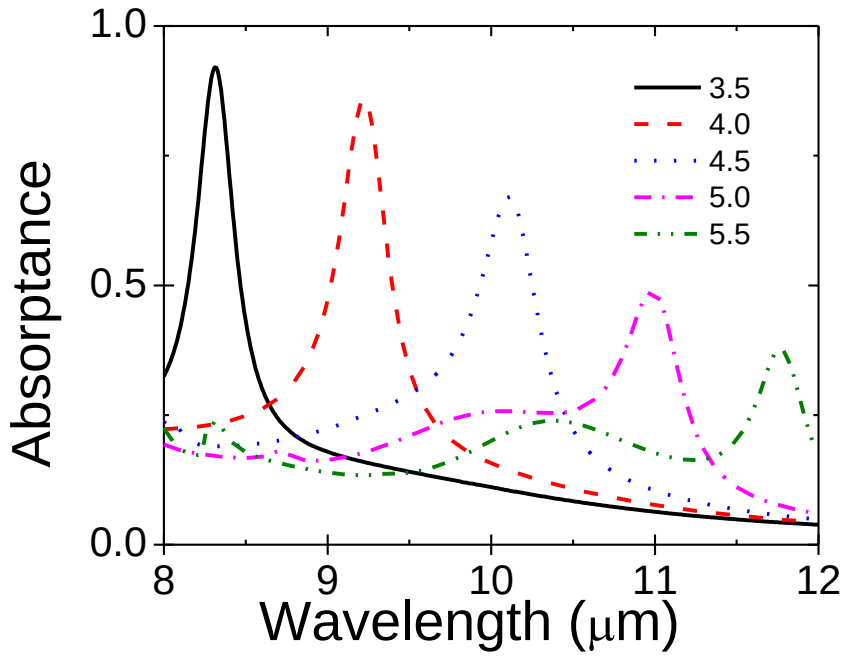

Fig. 6.2 – Performance of a series of T2SL GMR absorbers with F = 0.75, d_h = 0.5 μm, d_g = 1.27 μm, and 3.5 μm ≤ Λ ≤ 5.5 μm.

Figure 6.2 illustrates that by utilizing GMR we are able to achieve high absorption in a narrow band within the desired range. Furthermore, the device is shown to be tunable via periodicity. Unfortunately, the longer end of the band suffers from comparatively low absorption and the peak can be seen to diminish. To counter this, additional device families were explored. For a concise illustration we have chosen to demonstrate a family of curves operable at longer wavelengths

that follow F = 0.68, d_g = 0.0, d_g = 1.77, and 5 ≤ Λ ≤ 7. Figure 6.3 illustrates these results showcasing a grating topology that is more effective at longer wavelengths.

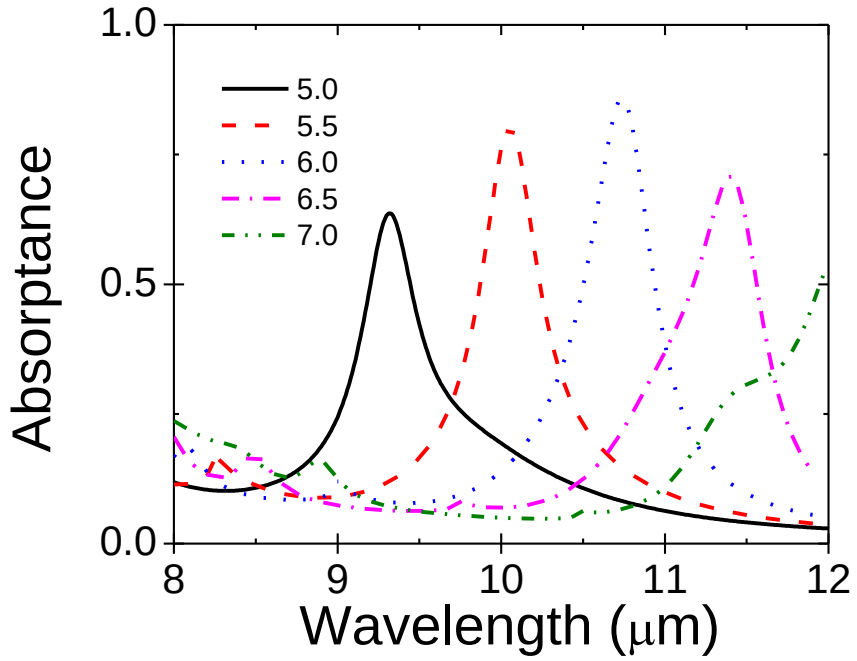

Fig. 6.3 - Performance of a series of T2SL GMR absorbers with F = 0.68, d_g = 0.0 μm, d_g = 1.77 μm, and 5 μm ≤ Λ ≤ 7 μm. The optimal location is near 11 μm where the absorption coefficient of the T2SL is comparatively lower than at the shorter wavelengths.

Figures 6.2 and 6.3 clearly illustrate some of the classical strengths of GMR devices including their strong resonant responses and tunability applied to the mid IR band. These initial results give a strong indication that they will operate quite similarly to their plasmonic counterparts trading off some bandwidth for some gains in absorptance. In the interest of investigating similar topologies we

investigate the same device family presented in Fig. 6.2 with cylindrical features in place of rectangular prisms.

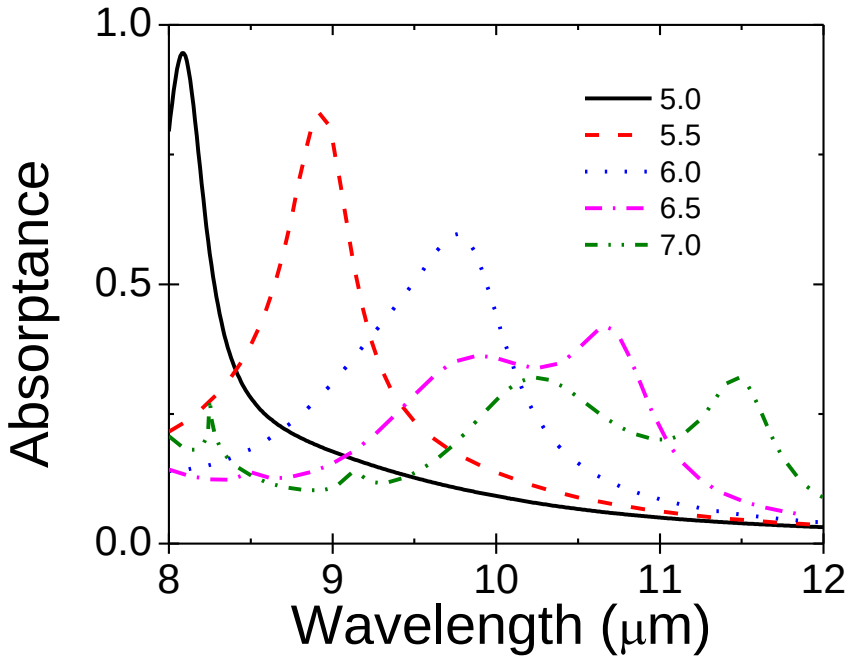

Fig. 6.4 – Same device from Fig. 6.2 with cylindrical features.

From Fig. 6.4 one can see that the majority of features are retained for the cylindrical case as in the rectangular one with some minor blue shift and broadening of the peaks. Thus, we can reasonably conclude a theoretically desirable performance from a T2SL GMR based absorber in the mid IR which could be patterned with reasonable flexibility. Lastly, we investigate the possibility of

utilizing two different periodicities to create two resonant wavelengths in place of one. Such a design could be tailored to give a wider response or to be sensitive to two specific locations depending upon the application. Figure 6.5 illustrates one possible configuration resulting in two resonant peaks occurring at 7.89 µm and 9.8 µm. This occurrence is a result of dual periodicities in the design lending different polarizations to favor an individual peak. Figure 6.5 illustrates this concept by filtering the results based on polarization angle.

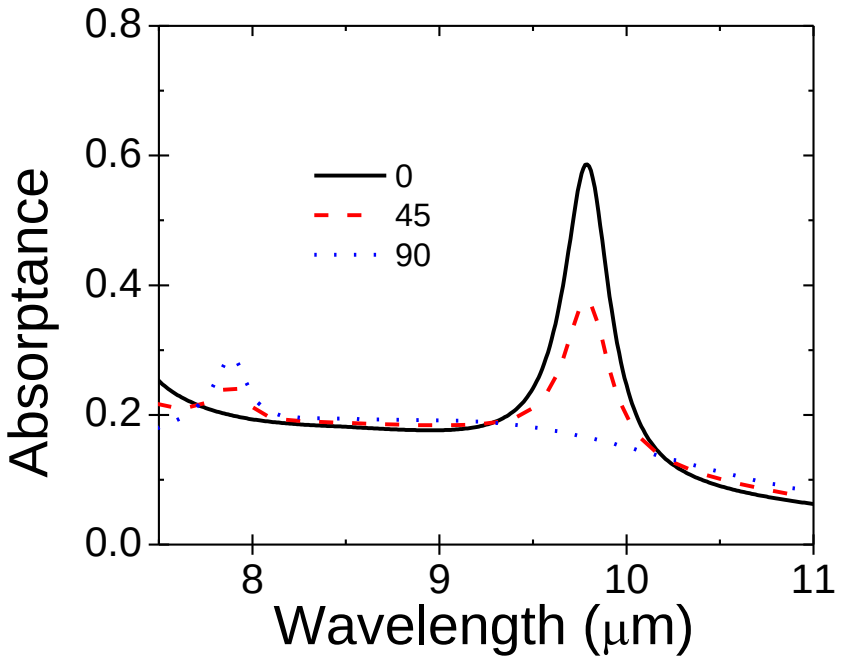

Fig. 6.5 – Absorptance curves based on polarization angle for a 2D T2SL with Λ_x = 3.2 µm, Λ_y = 4.4 µm, F = 0.75, d_h = 0.5 µm, and d_g = 1.2 µm.

6.3 Discussion and conclusions

The results from Fig. 6.5 illustrate one example of a dually periodic device with each polarization state favoring one peak over the other. This leads to an average response represented by the red dashed line for unpolarized incident light. Additional analysis could undoubtedly uncover more impressive results offering additional performance enhancements.

In conclusion, by leveraging the capabilities of GMR devices with 2D topologies and newer material profiles we have shown that, in theory, GMR is useful in the pursuit of highly absorbing thin film devices in the mid IR. By varying the critical dimensions of a device we show strong performance at both ends of the band. For each design, we have shown tunability via the periodicity representing operable devices across the entire band. Lastly, we conclude that multi-resonant topologies are theoretically achievable via differing periodicities in the lateral directions. These results compare favorably to plasmon enhanced topologies which suffer from ohmic losses and reduce the maximum available energy to the active part of the device.

Chapter 7

Future directions

7.1 Active CPA

In Chapter 2, an electrically readable CPA device was introduced as a future goal. The ability to electrically read input from optical devices is of particular interest in the telecommunications field, especially in high noise situations. CPA only works with coherent light implying high sensitivity to coherent signals. Applying an electrically readable topology to a similar device to the ones seen in Chapter 2 requires attention to both the electrical and optical properties. As a proof-of-concept, a design consisting of a hydrogenated amorphous silicon (a-Si:H) GMR element integrated with a pin junction in-between two layers of ITO for contacts was produced. Figures 7.1 and 7.2 illustrate the conceptual design and theoretical performance.

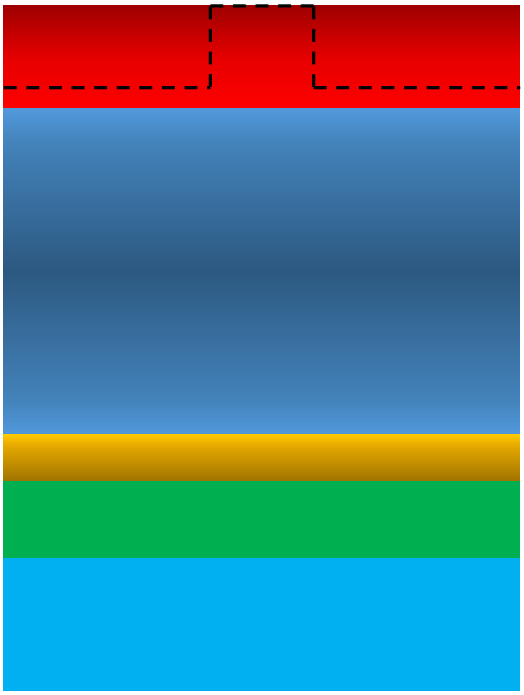

Fig. 7.1 – Active CPA model based on a-Si:H encapsulated by ITO contacts on glass.

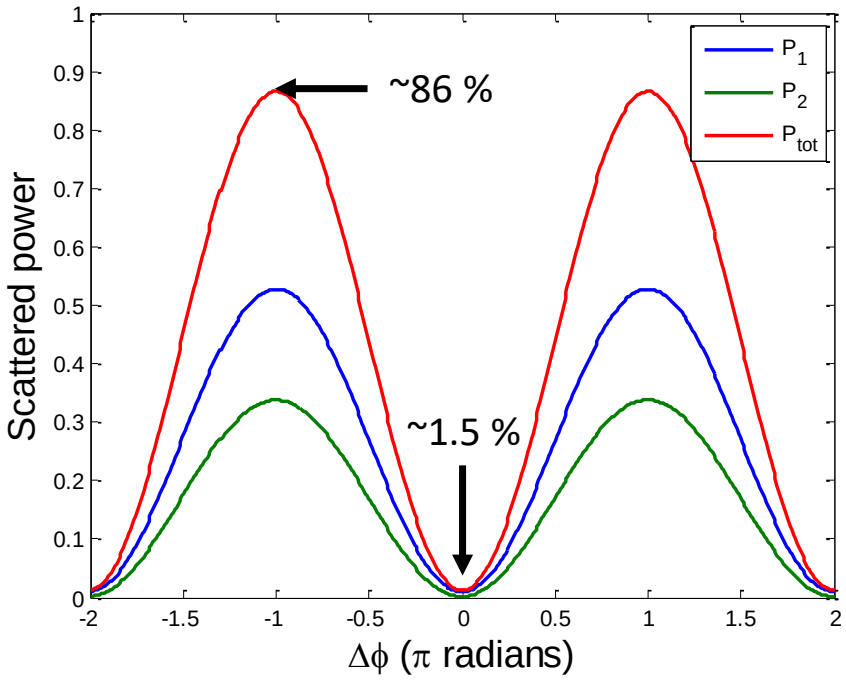

Fig. 7.2 – Theoretical performance of the active CA device from Fig. 7.1.

Figures 7.1 and 7.2 indicate the ability to, in theory, create electrically readable CA devices. In practice, the fabricated device was shown to perform well electrically in the visible. At telecom wavelengths, where the device is designed to operate, the performance at 1300 nm was detectable, but quite weak, requiring higher power incident light to be detected. In the experimental setup, the maximum output power was found to be well below that which was necessary to detect any changes electrically. Even still, the optical properties were tested. Figure 7.3 illustrates the devices performance.

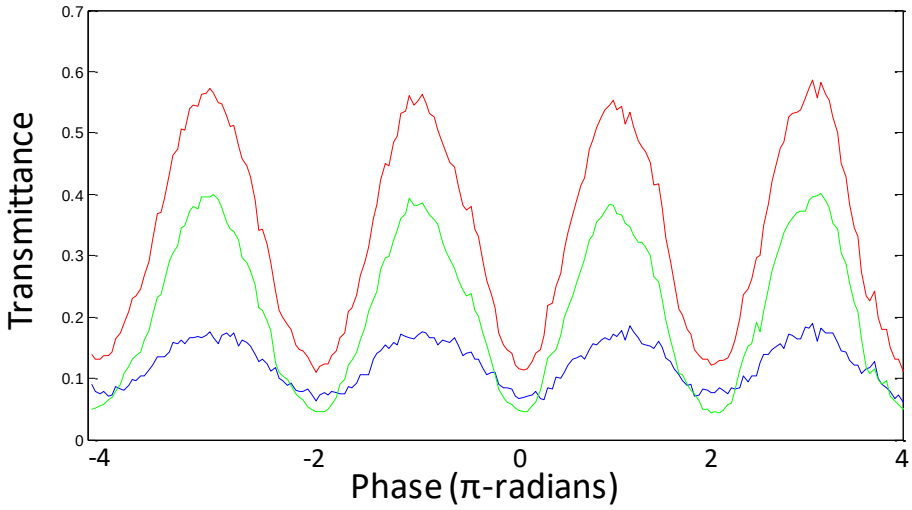

Fig. 7.3 – Experimental active CPA device performance at 1371 nm.

Similar to the results from Chapter 2, the active CPA device suffers from beam divergence despite the addition of several beam shaping elements demonstrating the devices sensitivity to beam divergence. Additionally, neither the theoretical minimum of 1.5% or maximum of 86% were achieved. Nevertheless, the device clearly illustrates the desired effect operating on the diode structure with a respectable amount of swing between the minimum at about 10% and the maximum at about 58%. Future work on this class of device could focus on bringing the minimum transmittance down as well as enhancing the electrical properties. Perhaps the easiest way to achieve both would be to blue-shift to another wavelength where the absorption coefficient of silicon is higher.

Another point worth exploring in the GMR based CPA field is the use of multiple resonances within the same device tuned by angle. In other words, the GMR wavelength

can be shifted by altering the angle at which light is applied to the device. Thus, a single device, in theory, should be capable of processing multiple signals in parallel. In the case of an active device, this technique would distort the electrical signal unless each signal was spaced temporally. In either case, one possible but relatively unexplored aspect of GMR based CPA devices is the ability for one device to handle multiple signals without cross-talk.

7.2 Low index Rayleigh sensors

There are several devices of interest from Chapter 3, the most practical of which is the low index biosensor. Developing a device concept capable of capitalizing on the gains of the low index sensor in both TE and TM polarizations would be beneficial. Furthermore, the device should be producible, excited and interrogated via the substrate, and operated within the same band as commercial systems. All of the above would prove beneficial in real world devices and applications without requiring modification or addition to equipment currently in use. For the most part, the design and fabrication techniques for producing such a device our outlined in Chapter 3. Additional computational methods may be warranted to further optimize the system. In the pursuit of this work, a similar but more difficult to realize topology was investigated with some merit. Namely, the ability to fabricate subwavelength grating elements with metallic layers embedded within the trenches may be of interest to future research. A fabrication

plan for such device is outlined below and may be of interest in the future for hybrid devices.

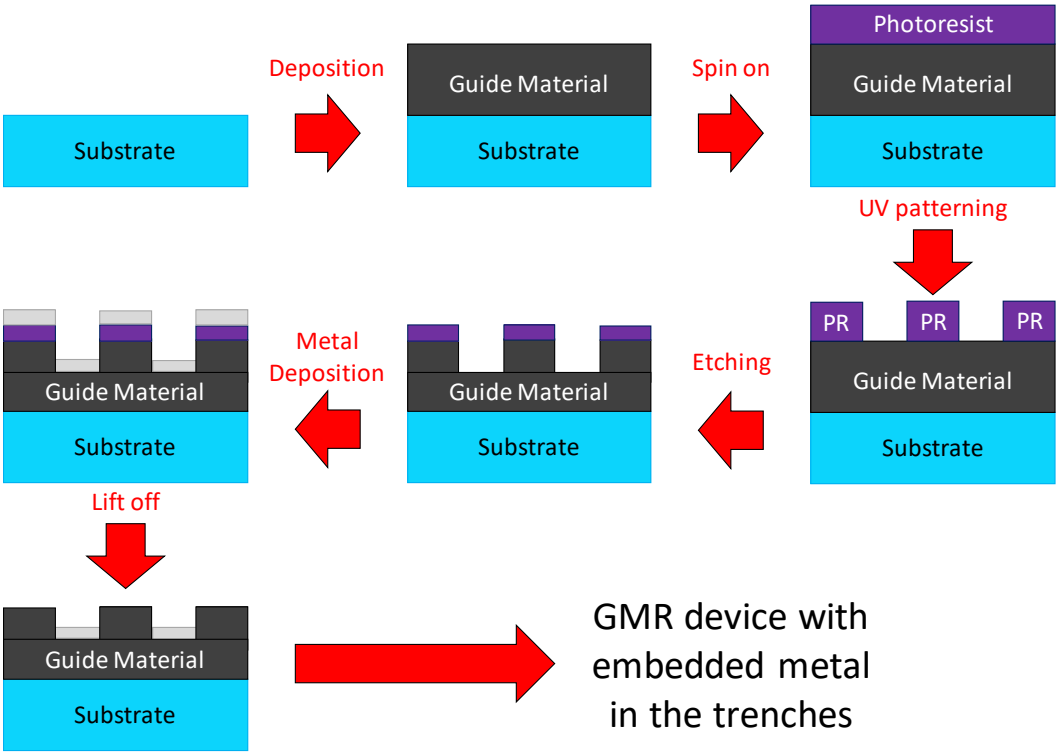

Fig. 7.4 - Fabrication plan for a mixed metal-dielectric GMR device with embedded metal in the trenches.

Further study on how to capitalize on the unique structure could also be of merit. Like the sensor discussed in Chapter 3, devices with this topology are able to draw upon strong GMR effects behind the substrate Rayleigh wavelength making it a somewhat unique operating regime. The inclusion of metals on dielectric materials further opens the door to mixed GMR-plasmonic interactions that may be of interest. In total, the device

offers many unique interactions reliant upon several different phenomena that may be of use individually or collectively.

7.3 2D fabrication techniques and device concepts

The pursuit of polarization insensitive GMR devices has led to the investigation of two-dimensional (2D) topologies. It has been shown here, at least for some topologies, that a one-dimensional (1D) design can be expanded into 2D directly with minimal impact on the resulting spectrum. Furthermore, it has been shown that either the TE or TM polarized response for the 1D equivalent can be emphasized based upon the scheme chosen for the 2D expansion. While based on the same fundamentals, 2D designs contain more parametric combinations than their one-dimensional counterparts. For instance, the periodicity in both the x and y directions can be varied independently.

2D topologies are also of interest in the fabrication of small localized surface plasmon resonant (LSPR) devices. It was recently found that laser interference lithography (LIL) could be used to fabricate highly ordered arrays of metallic nanoparticles, usually gold nanoparticles (GNP) [1]. The ability to create large area GNP arrays can be of use in absorbers, surface enhanced Raman scattering applications, and even for making masks for high aspect ratio designs utilizing metal assisted etching [2].

Previous work by Yoon et. al. illustrated a 1D GMR based wideband absorber that exhibited polarization insensitivity [3]. The design was based on a-Si and had the dimensions of $\Lambda = 400$ nm, $d_g = 4$ μm, $d_h = 0.8$ μm, and $F = 0.25$. The device specifications, most notably the aspect ratio of 40:1, proved quite difficult to achieve resulting in an experimental device with an etch depth of only 2 μm. The homogenous layer was maintained at 0.8 μm. This reduced the aspect ratio to 20:1 but had a detracting effect on the overall performance. Even still, the design achieved strong absorption across the visible region. The depth was achieved using a deep reactive ion etcher (DRIE). To provide a fair comparison to other designs we have computed additional simulations based on the given description using rigorous coupled wave analysis (RCWA).

While the performance of the 1D device described is desirable for numerous applications, it would be more convenient if a similarly performing device could be made with a lower aspect ratio. To investigate possible solutions we have chosen to limit the maximum height of the absorbing layer to 2 μm, the etch depth achieved in the 1D device. This ensures that any design unveiled, provided that the aspect ratio is no larger than the 20:1 achieved in the 1D device, can be fabricated utilizing the same techniques used by Yoon et. al. Furthermore, a periodicity of 460 nm is chosen as the minimum for each design to ensure that laser interference lithography (LIL) can be safely utilized to create the structures.

The 1D device is optimized for the visible region requiring any new topologies comprised of the same materials to be 2D. A series of forward and inverse numerical methods are utilized to examine possible structures. A resulting topology is described as having a periodicity of 460 nm in x and y with a fill factor of 0.25 and 0.6 in x and y respectively. The resulting rectangular shape is found to have desirable performance at 1.7 μm tall, well within the limits previously discussed. The remaining 0.3 μm forms a homogenous layer beneath the grating structure. Corresponding spectral absorbance results can be seen in Fig. 7.5.

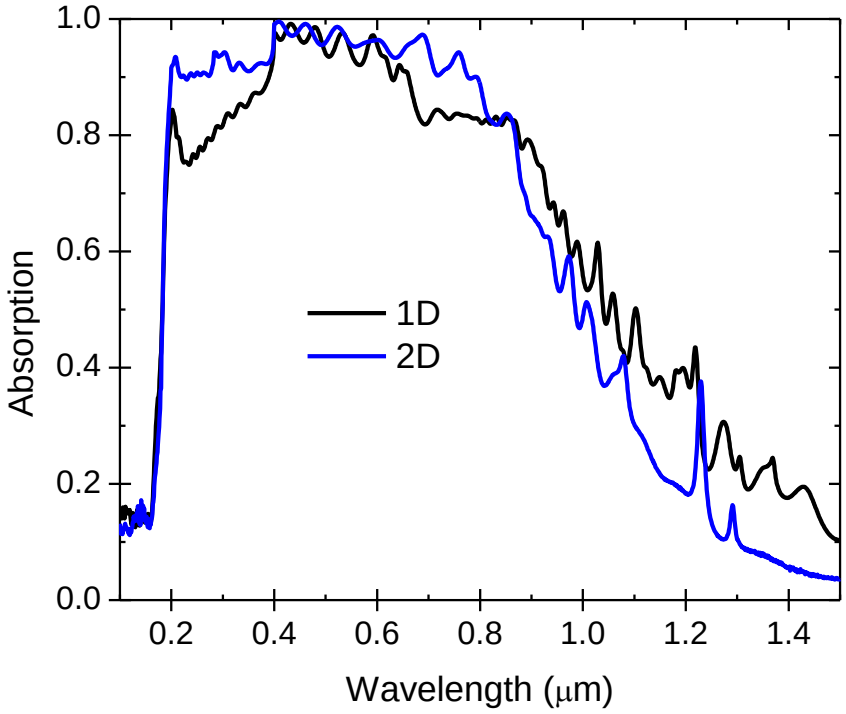

Fig. 7.5 - Comparative performance between the 1D and 2D wideband structures.

The results in Fig. 7.5 illustrate comparable performance with the original device. The aspect ratio is reduced to 14.8:1 thanks in part to the larger periodicity and more shallow grating height. In total, this conversion represents marginal gains for this family of devices. While the aspect ratio is more realizable, the 1.7 μm target etch depth would still, in all likelihood, need to be performed by a DRIE. For most fabrication facilities, it would be more convenient if such a device could be etched using a RIE. To further explore options for achieving such a goal, additional architectures are explored.

Expanding into 2D offers several additional parameters that have been discussed. These include periodicity and fill factor in x and y. It is found that the etch depth in x and y can also be varied offering 2D GMR devices comprised of three or four different heights. In short, a regular 1D grating mask can be generated using LIL and etched with an RIE. From there, an additional 1D mask can be generated atop the previous grating running in the perpendicular direction. Etching this mask with an RIE will yield a device with three steps or four steps depending on the etch time of each mask. Figure 7.6 illustrates this hypothetical topology.

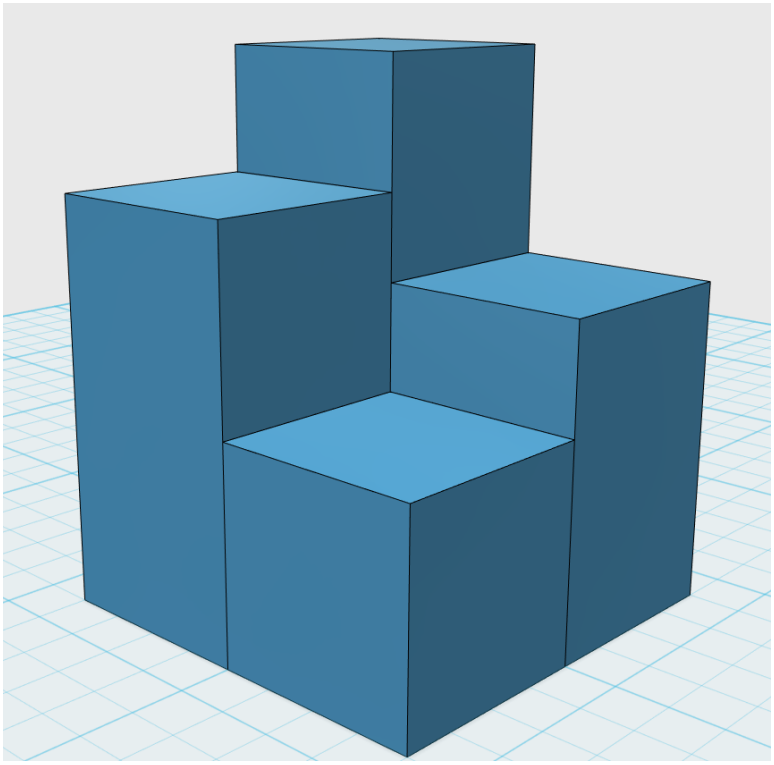

Fig. 7.6 - Design concept for a double etch GMR.

The proposed topology is dubbed as a double-etch (DE) GMR grating. A DE GMR offers a designer parametric variation of periodicity, fill factor, and etch depth in both the x and y directions. To focus efforts in optimizing such an involved topology an additional limit is imposed on the parameter set in addition to the ones defined previously for the 2D device. The limit reduces the maximum etch for a single mask to only 500 nm, an etch depth routinely achieved by our in-house RIE. Doing so ensures that any theoretical device studied could realistically be fabricated. Figure 7.7 illustrates our findings for a DE

GMR device with a periodicity of 460 nm in both x and y, a fill factor of 0.25 in both x and y, and an etch depth of 250 nm and 500 nm in x and y respectively.

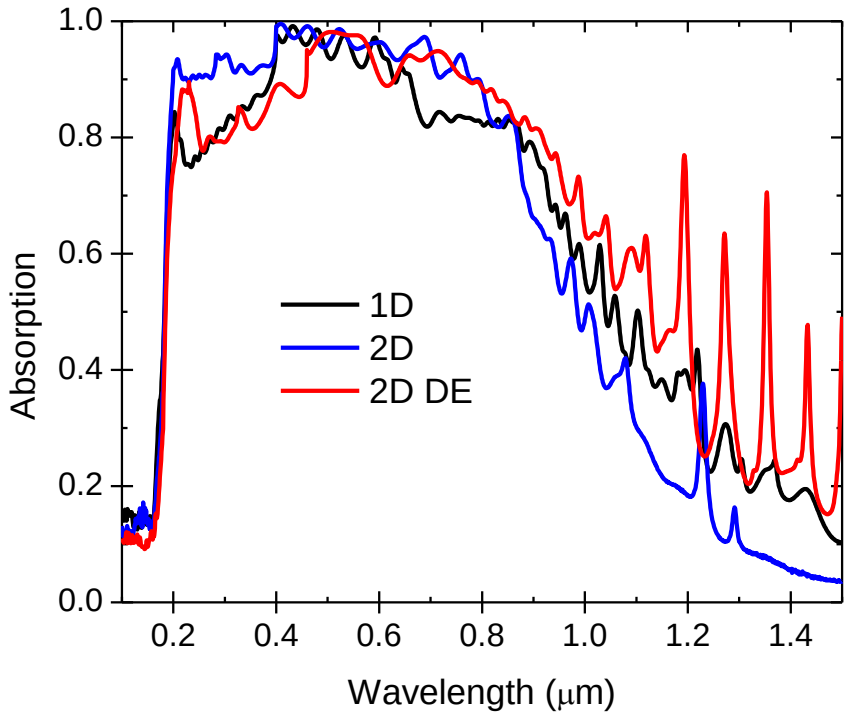

Fig. 7.7 - Comparison of the three wideband topologies discussed.

The results in Fig. 7.7 are once again comparable to the findings in Fig. 7.5. The benefit of moving to the DE design is that the aspect ratio is further reduced to 6.5:1, less than a third of the original 1D device. Furthermore, the device can theoretically be achieved using a RIE as opposed to a DRIE making the design more appealing to lesser equipped facilities. Table 7.1 accompanies Fig. 7.7 in comparing the three designs.

Table 7.1 - Comparison of wideband designs

	1D	2D	2D DE
Aspect Ratio	20.0:1	14.8:1	6.5:1
Absorption (0.4-0.7 μm)	0.94	0.97	0.93
Absorption (0.1-1.5 μm)	0.61	0.59	0.66

While the DE GMR device looks appealing in theory, it is questionable as to whether such a device can be realistically fabricated. As a proof of concept, a device is made using the process outlined previously. It is found that the design utilized is difficult to reliably fabricate. For the purposes of evaluating the fabrication technique, several parameters are changed. The periodicity is enlarged to 600 nm in both x and y while the etch depth in the x direction is reduced to 150 nm. The resulting device is measured via atomic force microscopy (AFM). Figure 7.8 illustrates the design proof of concept.

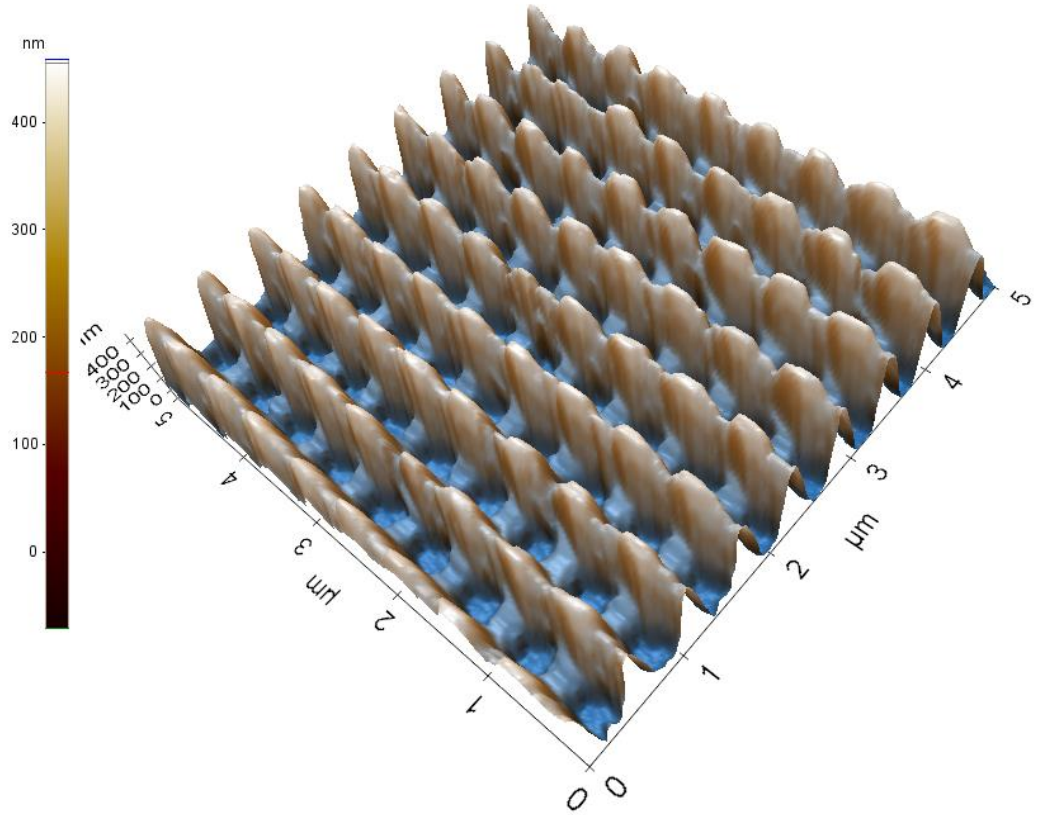

Fig. 7.8 - AFM image of a proof of concept DE GMR device.

These preliminary results indicate that the DE GMR concept is indeed producible with larger feature sizes. The design in Fig. 7.8 can be shown to operate primarily in the NIR from about 800 nm – 1100 nm. Further work will be necessary to create a functioning device in the visible band.

In addition to the wideband absorber, topologies that utilize 2D structures are of interest. Specifically, GNP arrays are a topic of interest as they can be applied to various areas including surface-enhanced Raman spectroscopy and solar cell enhancement. GNP

arrays are typically fabricated using aqueous solutions. This makes them difficult to adhere to surfaces. Recently, it was shown that GNP arrays could be made using LIL techniques [1]. Using a similar method, we have confirmed LIL as a practical method for fabricating large area arrays of GNP. Furthermore, we have also confirmed the potential for fabricating ellipsoidal GNP arrays. Figure 7.9 illustrates several of the resulting topologies.

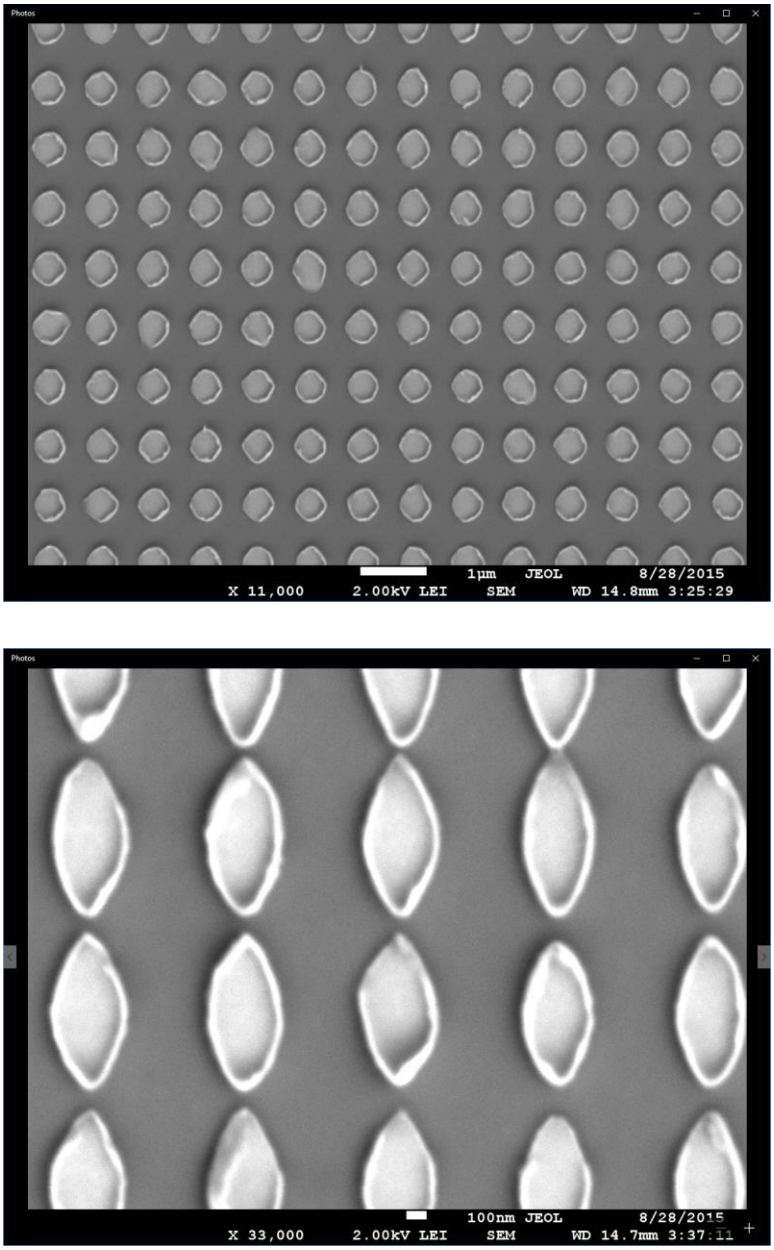

Fig. 7.9 - Sample GNP arrays produced by sputtering gold atop a PR mask generated by LIL.

The results from Fig. 7.9 are of interest as GNP arrays can be utilized to foster LSPR effects. Combining principles of GNP arrays and GMR devices could be of interest in

various fields. Since the GNP arrays from Fig. 7.9 are created via sputtering, they adhere to planar surfaces quite well. A question of interest is whether they could be adhered to rough surfaces or even gratings. To investigate this concept, a simple grating is formed using LIL to create a mask in crystalline silicon. The resulting mask is etched into the silicon about 250 nm. An additional PR masked is formed utilizing 2D LIL and subsequently sputtered with gold. After a lift-off procedure the resulting device is examined under an SEM. Figure 7.10 illustrates the results.

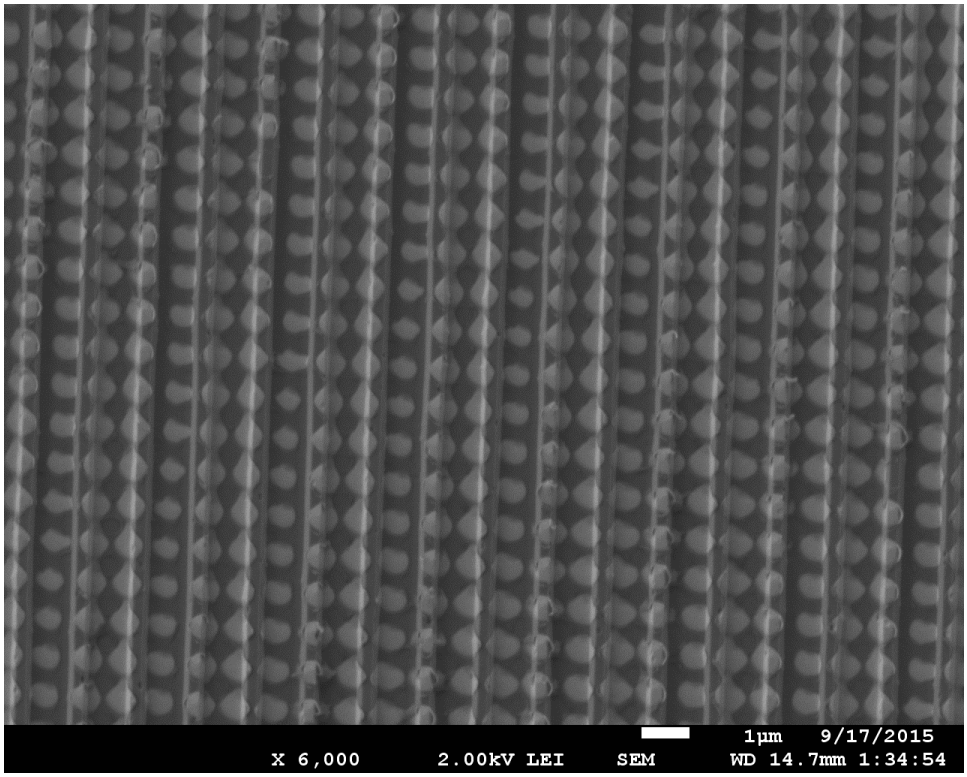

Fig. 7.10 - A GNP array formed by LIL adhered to a silicon grating.

The ability to fabricate GNP arrays atop grating structures represents potential gains in device engineering as it implies optimized structures utilizing GNP arrays or GMR structures can be combined independently.

7.4 Ultra-wideband GMR-plasmonic absorbers

The last device type that will be discussed is a variant of the wideband absorber proposed in Chapter 4. The device described in Chapter 4, while interesting, cannot claim to be novel as it simply expands previous work. Here we modify the design to incorporate plasmonics to extend the operation into the near- to mid-IR bands. While interesting, this concept is only explored briefly. In short, by utilizing the technique for depositing structured metal nanoparticles detailed previously in conjunction with a conformal deposition process, a hybrid GMR-plasmonic device can be modeled. Furthermore, the plasmonic activity would occur near the center of the dielectric film implying potential use for photodetection and harvesting. Lastly, the plasmonic properties would be tuned to the near and mid IR region where they enable wideband effects. Figure 7.11 illustrates a sample topology of this device type.

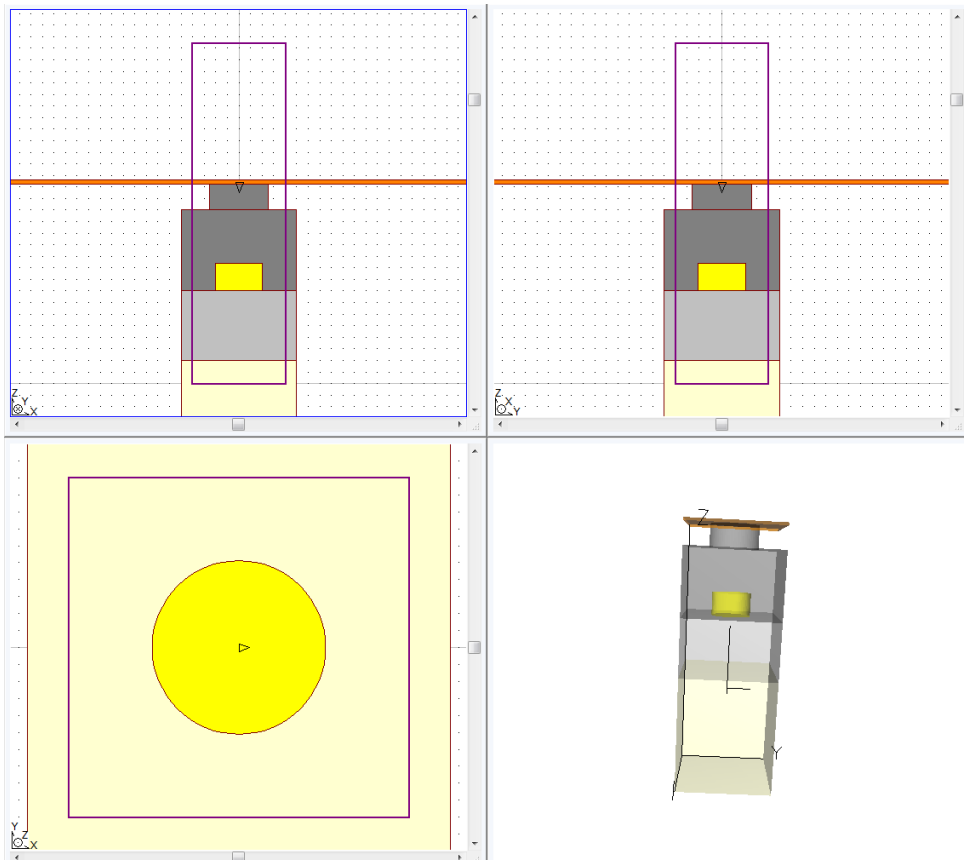

Fig. 7.11 – Sample device structure for an ultra-wideband GMR-plasmonic absorber. Λ = 400 nm, F = 0.64, d_h = 350 nm, and d_g = 120 nm. The gold cylinder in the middle of the design is of the same height as the grating but has F = 0.8 d_g.

From simulations done on the device from Fig. 7.11 we note that the majority of SPR effects are concentrated atop the metallic cylinder, in the middle of the design. Preliminary performance increases between the purely GMR device and the hybrid device are illustrated in Fig. 7.12. In short, we find that the basic signature from the GMR device can remain mostly undisturbed whilst the SPR effects can be utilized to achieve additional gains in the near IR.

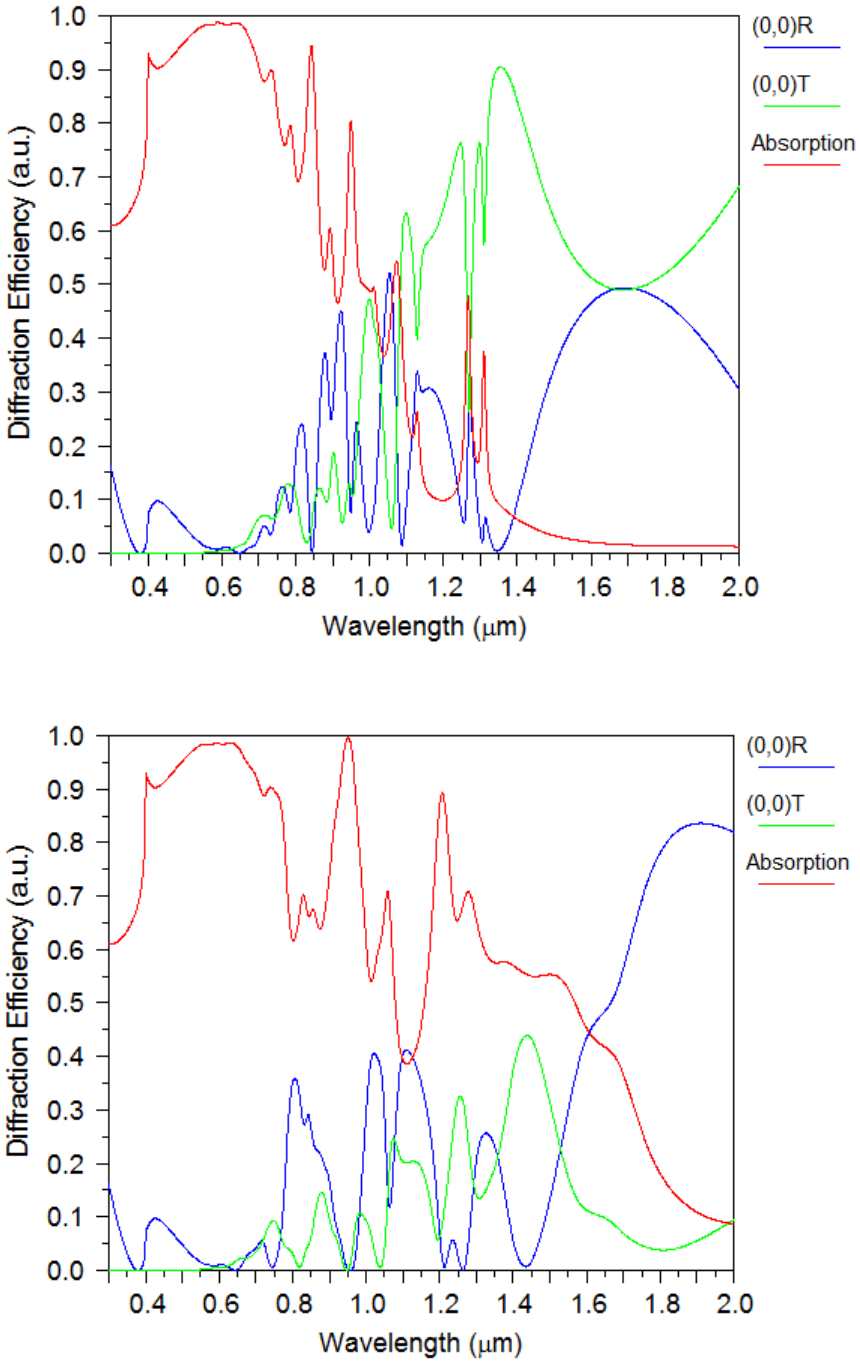

Fig. 7.12 – (Top) original devices performance across the visible and near IR. (Bottom) Preliminary results of the device from Fig. 7.11.

7.5 Conclusions

In conclusion, 2D patterning while expanding into the 3rd dimension (vertical direction) can be of significant use in devices as discussed briefly. Uses can include the elimination of polarization sensitivity, enhanced performance, and even combining multiple devices into one. A simple 1D GMR grating is shown to have desirable characteristics as a wideband absorber. A 2D-to-3D expansion utilizing the same concept is shown to have moderately improved characteristics in performance while remaining amenable to fabrication with moderate aspect ratios. A 2D conceptual device is presented as a 2D double-etched GMR; it is really a 3D concept. Theoretical calculations imply that the conceptual device has similar performance with the 1D and 2D grating structures. The 2D double etch design is shown to aid in fabrication by reducing the aspect ratio from 20:1 to 6.5:1 implying that a RIE may be used in place of a DRIE. A proof-of-concept double etch design is fabricated utilizing LIL and a RIE and measured via AFM. Additional 2D topologies are explored utilizing GNP arrays on planar silicon surfaces. The arrays are formed by sputtering gold onto a PR mask made with LIL. The resulting particles are shown to be producible in both circular and elliptical shapes. Lastly, it is demonstrated that the GNP array fabrication technique utilized can be used to adhere GNP arrays onto non-planar surfaces, specifically a grating. This has applications in

surface-enhanced Raman spectroscopy and absorbing devices like solar cells and photodetectors.

List of Publications and Presentations

Fannin, A. L., J. W. Yoon, B. R. Wenner, J. W. Allen, M. S. Allen, and R. Magnusson, “Experimental Evidence for Coherent Perfect Absorption in Guided-Mode Resonant Silicon Films,” IEEE Photon. J. 8, 6802307 (2016).

Fannin, A. L., B. R. Wenner, J. W. Allen, M. S. Allen, and R. Magnusson, "Properties of mixed metal–dielectric nanogratings for application in resonant absorption, sensing, and display." Optical Engineering 56.12 (2017): 121905-121905.

Fannin, A. L., B. R. Wenner, J. W. Allen, M. S. Allen, and R. Magnusson, “Guided-mode resonance assisted ultra-sparse absorbing grating polarizers,” (to be submitted).

Presenter, “Optical Resonant Absorber Technology,” 3rd Nanosmat-USA 2016, May 18-20, 2016, Arlington, Tx.

Presenter, “Resonant Absorber Device Technology,” UT Arlington Photonics Symposium, Sept. 14, 2015, Arlington, Tx.

References

Chapter 1

[1] E. Hecht, *Optics*, 4th ed., Addison Wesley, San Francisco, 2002

[2] P. Vincent, and M. Neviere. "Corrugated dielectric waveguides: A numerical study of the second-order stop bands." Applied physics 20.4, 345-351 (1979).

[3] L. Mashev, and E. Popov. "Zero order anomaly of dielectric coated gratings." Optics communications 55.6, 377-380 (1985).

[4] G. A. Golubenko, et al. "Total reflection of light from a corrugated surface of a dielectric waveguide." Soviet journal of quantum electronics 15.7, 886 (1985).

[5] R. Magnusson and S. S. Wang, “New principle for optical filters,” Appl. Phys. Lett. 61, 1022–1024 (1992).

[6] S. S. Wang and R. Magnusson, “Theory and applications of guided-mode resonance filters,” Appl. Opt. 32, 2606-2613 (1993).

[7] D. Wawro, S. Tibuleac, R. Magnusson, and H. Liu, “Optical fiber endface biosensor based on resonances in dielectric waveguide gratings,” Proc. SPIE 3911, 86-94 (2000).

[8] H. Kikuta, N. Maegawa, A. Mizutani, K. Iwata, and H. Toyota, “Refractive index sensor with a guided-mode resonant grating filter,” Proc. SPIE 4416, 219-222 (2001).

[9] R. Magnusson, D. Wawro, S. Zimmerman, and Y. Ding, “Resonant photonic biosensors with polarization-based multiparametric discrimination in each channel,” Sensors: Special Issue Opt. Resonant Sensors 11, 1476-1488 (2011).

[10] T. Khaleque, H. Svavarsson, and R. Magnusson, “Fabrication of resonant patterns using thermal nano-imprint lithography for thin-film photovoltaic applications,” Optics Express—Energy, 21, A631-A641, (2013).

[11] R. Magnusson, P. P. Young, and D. Shin, “Vertical-cavity laser and laser array incorporating guided-mode resonance effects and method for making the same,” U.S. patent number 6,154,480.

[12] M. G. Moharam and T. K. Gaylord, "Rigorous coupled-wave analysis of planar-grating diffraction," J. Opt. Soc. Am. 71, 811-818 (1981).

[13] A. Taflove, and S. C. Hagness. *Computational electrodynamics*. Artech house publishers, 2000.

[14] O. C. Zienkiewicz, et al, *The finite element method*, Vol. 3, London: McGraw-hill, 1977.

[15] J. Kennedy. "Particle swarm optimization." Encyclopedia of machine learning, Springer US, 2011. 760-766.

[16] Y. D. Chong, Li. Ge, H. Cao, and A. D. Stone, “Coherent perfect absorbers: time-reversed lasers,” Phys. Rev. Lett. 105, 053901 (2010).

[17] D. Mazulquim, K. J. Lee, J. W. Yoon, L. V. Muniz, B. V. Borges, L. G. Neto, and R. Magnusson, “Efficient band-pass color filters enabled by resonant modes and plasmons near the Rayleigh anomaly,” Opt. Express 22(25), 30843-30851 (2014).

[18] A. Mizutani, S. Urakawa, and H. Kikuta, “Highly sensitive refractive index sensor using a resonant grating waveguide on a metal substrate,” Applied Optics 54(13), 4161-4166 (2015).

[19] H. Raether, *Surface plasmons on smooth and rough surfaces and on gratings*, Springer, Verlag, Berlin (1988).

Chapter 2

[1] J. W. Yoon, K. J. Lee, W. Wu, and R. Magnusson, “Wideband omnidirectional polarization-insensitive light absorbers made with 1D silicon gratings,” Advanced Optical Materials 2, 1206-1212 (2014).

[2] F. Cheng, J. Gao, T. S. Suk, and X. Yang, “Structural color printing based on plasmonic metasurfaces of perfect light absorption,” Scientific Reports 5, 11045 (2015).

[3] Y. D. Chong, Li. Ge, H. Cao, and A. D. Stone, “Coherent perfect absorbers: time-reversed lasers,” Phys. Rev. Lett. 105, 053901 (2010).

[4] J. Yoon, K. H. Seol, S. H. Song, and R. Magnusson, “Critical coupling in dissipative surface-plasmon resonators with multiple ports,” Opt. Express 18, 25702–25711 (2010).

[5] J. Zhang, K. F. MacDonald, and N. I. Zheludev, “Controlling light-with-light without nonlinearity,” Light: Science & Applications 1, 1–5 (2012).

[6] X. Fang, K. F. MacDonald, and N. I. Zheludev, “Controlling light with light using coherent metadevices: all-optical transistor, summator, and invertor,” Light: Science & Applications 4, e292 (2015).

[7] W. Wan, Y. Chong, L. Ge, H. Noh, A. D. Stone, and H. Cao, “Time-reversed lasing and interferometric control of absorption,” Science 331, 889–892 (2011).

[8] J. W. Yoon, G. M. Koh, S. H. Song, and R. Magnusson, “Measurement and modeling of a complete optical absorption and scattering by coherent surface plasmon-polariton excitation using a silver thin-film grating,” Phys. Rev. Lett. 109, 257402 (2012).

[9] R. R. Grote, J. M. Rothenberg, J. B. Driscoll and R. M. Osgood, "DPSK demodulation using coherent perfect absorption," 2015 Conference on Lasers and Electro-Optics (CLEO), 1-2, (2015).

[10] J. Zhang, C. Guo, K. Liu, Z. Zhu, W. Ye, X. Yuan, and S. Qin, "Coherent perfect absorption and transparency in a nanostructured graphene film," Opt. Express 22, 12524-12532 (2014).

[11] S. Feng and K. Halterman, “Coherent perfect absorption in epsilon-near-zero metamaterials,” Phys. Rev. B 86(16), 165103 (2012).

[12] J. A. Giese, J. W. Yoon, B. R. Wenner, J. W. Allen, M. S. Allen, and R. Magnusson, “Guided-mode resonant coherent light absorbers,” Opt. Lett. 39(3), 486–488 (2014).

[13] P. Vincent and M. Neviere, “Corrugated dielectric waveguides: A numerical study of the second-order stop bands,” Appl. Phys. 20, 345–351 (1979).

[14] L. Mashev and E. Popov, “Zero order anomaly of dielectric coated gratings,” Opt. Comm. 55, 377–380 (1985).

[15] I. A. Avrutsky and V. A. Sychugov, “Reflection of a beam of finite size from a corrugated waveguide,” J. Mod. Opt. 36, 1527–1539 (1989).

[16] S. S. Wang and R. Magnusson, “Theory and applications of guided-mode resonance filters,” Appl. Opt. 32, 2606–2613 (1993).

[17] S. T. Thurman and G. M. Morris, "Controlling the spectral response in guided-mode resonance filter design," Appl. Opt. 42, 3225-3233 (2003).

[18] Y. Ding and R. Magnusson, “Resonant leaky-mode spectral-band engineering and device applications,” Opt. Express 12, 5661–5674 (2004).

[19] Z. Wang, T. Sang, L. Wang, J. Zhu, Y. Wu, and L. Chen, “Guided-mode resonance Brewster filters with multiple channels,” Appl. Phys. Lett. 88(25), 251115 (2006).

[20] Y. Lee, C. Huang, J. Chang, and M. Wu, "Enhanced light trapping based on guided mode resonance effect for thin-film silicon solar cells with two filling-factor gratings," Opt. Express 16, 7969-7975 (2008).

[21] S. Boonruang, A. Greenwell, and M. G. Moharam, "Multiline two-dimensional guided-mode resonant filters," Appl. Opt. 45, 5740-5747 (2006).

[22] E. Sakat, G. Vincent, P. Ghenuche, N. Bardou, C. Dupuis, S. Collin, F. Pardo, R. Haïdar, and J. Pelouard, "Free-standing guided-mode resonance band-pass filters: from 1D to 2D structures," Opt. Express 20, 13082-13090 (2012).

[23] W. Zhou, D. Zhao, Y.-C. Shuai, H. Yang, S. Chuwongin, A. Chadha, J.-H. Seo, K. X. Wang, V. Liu, Z. Ma, and S. Fan, “Progress in 2D photonic crystal Fano resonance photonics,” Prog. Quantum Electron 38, 1–74 (2014).

Chapter 3

[1] P. Vincent and M. Neviere, “Corrugated dielectric waveguides: A numerical study of the second-order stop bands,” Appl. Phys., vol. 20, no. 4, 345-351, (1979).

[2] L. Mashev and E. Popov, “Zero order anomaly of dielectric coated gratings,” Opt. Comm., vol. 55, no. 6, 377-380, Oct. 15, (1985).

[3] E. Popov, L. Mashev, and D. Maystre, “Theoretical study of anomalies of coated dielectric gratings,” J. Mod. Opt., vol. 33, no. 5, 607–619, May (1986).

[4] G. A. Golubenko, A. S. Svakhin, V. A. Sychugov, and A. V. Tishchenko, “Total reflection of light from a corrugated surface of a dielectric waveguide,” Sov. J. Quantum Electron., vol. 15, no. 7, 886-887, (1985).

[5] I. A. Avrutsky and V. A. Sychugov, “Reflection of a beam of finite size from a corrugated waveguide,” J. Mod. Opt., vol. 36, no. 11, 1527-1539, Nov. (1989).

[6] R. Magnusson and S. S. Wang, “New principle for optical filters,” Appl. Phys. Lett., vol. 61, no. 9, 1022-1024, Aug. (1992).

[7] S. S. Wang and R. Magnusson, “Theory and applications of guided-mode resonance filters,” Appl. Opt., vol. 32, no. 14, 2606-2613, May 10, (1993).

[8] Y. Ding and R. Magnusson, "Resonant leaky-mode spectral-band engineering and device applications," Opt. Express 12, 5661-5674 (2004).

[9] D. Wawro, S. Tibuleac, R. Magnusson, and H. Liu, “Optical fiber endface biosensor based on resonances in dielectric waveguide gratings,” Proc. SPIE 3911, 86-94 (2000).

[10] H. Kikuta, N. Maegawa, A. Mizutani, K. Iwata, and H. Toyota, “Refractive index sensor with a guided-mode resonant grating filter,” Proc. SPIE 4416, 219-222 (2001).

[11] J. J. Wang, L. Chen, S. Kwan, L. Feng, and X. Deng, “Resonant grating filters as refractive index sensors for chemical and biological detections,” J. Vac. Sci. Technol. B 23, 3006-3010 (2005).

[12] R. Magnusson, D. Wawro, S. Zimmerman, and Y. Ding, “Resonant photonic biosensors with polarization-based multiparametric discrimination in each channel,” Sensors: Special Issue Opt. Resonant Sensors 11, 1476-1488 (2011).

[13] H. Raether, *Surface plasmons on smooth and rough surfaces and on gratings*, Springer Berlin Heidelberg (1988).

[14] S. A. Maier, *Plasmonics: fundamentals and applications*, Springer Science and Business Media, New York (2007).

[15] S. Enoch and N. Bonod, eds. *Plasmonics: from basics to advanced topics*, Vol. 167, Springer (2012).

[16] R. W. Wood, “XLII. On a remarkable case of uneven distribution of light in a diffraction grating spectrum,“ The London, Edinburgh, and Dublin Philosophical Magazine and Journal of Science 4.21, 396-402 (1902).

[17] D. Maystre, ‘Theory of Wood’s Anomalies’, *Plasmonics: from basics to advanced topics,* Vol. 167, Springer, 39-83 (2012).

[18] J. Homola, S. S. Yee, and G. Gauglitz, “Surface plasmon resonance sensors: review,” Sensors and Act. B 54(1-2), 3-15 (1999).

[19] J. Homola, “Present and future of surface plasmon resonance biosensors,” Anal. Bioanal. Chem. 377, 528-539 (2003).

[20] S. Roh, T. Chung, and B. Lee, “Overview of the characteristics of micro- and nano-structured surface plasmon resonance sensors,” Sensors 11(2), 1565-1588 (2011).

[21] S. Pillai, K. R. Catchpole, T. Trupke and M. A. Green, “Surface plasmon enhanced silicon solar cells,” Journal of Applied Physics 101, 093105 (2007).

[22] D. Mazulquim, K. J. Lee, J. W. Yoon, L. V. Muniz, B. V. Borges, L. G. Neto, and R. Magnusson, “Efficient band-pass color filters enabled by resonant modes and plasmons near the Rayleigh anomaly,” Opt. Express 22(25), 30843-30851 (2014).

[23] J. Li, D. Fattal, and Z. Li, “Plasmonic optical antennas on dielectric gratings with high field enhancement for surface enhanced Raman spectroscopy,” Appl. Phys. Lett. 94, 263114 (2009).

[24] X. Xu, D. Hasan, L. Wang, S. Chakravarty, R. T. Chen, D. L. Fan, and A. X. Wang, “Guided-mode-resonance-coupled plasmonic-active SiO_2 nanotubes for surface enhanced Raman spectroscopy,” Appl. Phys. Lett. 100, 191114 (2012).

[25] A. Christ, S. G. Tikhodeev, N. A. Gippius, J. Kuhl, and H. Giessen, “Waveguide-plasmon polaritons: strong coupling of photonic and electronic resonances in a metallic photonic crystal slab,” Physical Review Letters 91, 183901 (2003).

[26] T. Zentgraf, S. Zhang, R. F. Oulton, and X. Zhang, “Ultranarrow coupling-induced transparency bands in hybrid plasmonic systems,” Phys. Rev. B 80, 195415 (2009).

[27] J. Zhang, L. Cai, W. Bai, and G. Song, "Hybrid waveguide-plasmon resonances in gold pillar arrays on top of a dielectric waveguide," Opt. Lett. 35, 3408-3410 (2010).

[28] C. Tan, J. Simonen, and T. Niemi, “Hybrid waveguide-surface plasmon polariton modes in a guided-mode resonance grating,” Optics Communications 285(21-22), 4381-4386 (2012).

[29] R. Magnusson, J. Yoon, and D. Wawro, “Properties of resonant modal-plasmonic multiparametric biosensors,” Proc. SPIE. 8570, 8700K (2013).

[30] M. G. Moharam and T. K. Gaylord, "Rigorous coupled-wave analysis of planar-grating diffraction," J. Opt. Soc. Am. 71, 811-818 (1981).

[31] P. B. Johnson and R. W. Christy, “Optical constants of the noble metals,” Phys. Rev. B 6(12), 4370-4379 (1972).

[32] R. Magnusson and S. S. Wang, “Optical guided-mode resonance filter,” U.S. patent number 5,216,680, issued June 1, (1993).

[33] S. Tibuleac, D. Wawro, and R. Magnusson, “Resonant diffractive structures integrating waveguide gratings on optical fiber endfaces,” Proc. IEEE 2, 874-875 (1999).

[34] B. Cunningham, P. Li, B. Lin, and J. Pepper, “Colorimetric resonant reflection as a direct biochemical assay technique,” Sensors and Actuators B 81, 316-328 (2002).

[35] B. Cunningham, B. Lin, J. Qiu, P. Li, J. Pepper, and B. Hugh, “A plastic colorimetric resonant optical biosensor for multiparallel detection of label-free biochemical interactions,” Sensors and Actuators B 85, 219-226 (2002).

[36] Y. Fang, A. M. Ferrie, and G. Li, “Probing cytoskeleton modulation by optical biosensors,” FEBS Letters 579, 4175-4180 (2005).

[37] Y. Fang, A. G. Frutos, and R. Verklereen, “Label-Free Cell-Based Assays for GPCR Screening,” Combinatorial Chemistry & High Throughput Screening, 357-369 (2008).

[38] A. Mizutani, S. Urakawa, and H. Kikuta, "Highly sensitive refractive index sensor using a resonant grating waveguide on a metal substrate," Appl. Opt. 54, 4161-4166 (2015).

[39] H. S. Lee, Y. T. Yoon, S. S. Lee, S. H. Kim, K. D. Lee, “Color filter based on a subwavelength patterned metal grating,” Opt. Express 15(23), 15457-15463 (2007).

[40] Y. T. Yoon and S. S. Lee, “Transmission type color filter incorporating a silver film based etalon,” Opt. Express 18(5), 5344-5349 (2010).

[41] M. J. Uddin and R. Magnusson, “Efficient guided-mode resonant tunable color filter,” IEEE Phot. Technol. Lett. 24(17), 1552-1554 (2012).

[42] Y. T. Yoon, C. H. Park, and S. S. Lee, “Highly efficient color filter incorporating a thin metal-dielectric resonant structure,” Appl. Phys. Express 5(2), 022501 (2012).

[43] A. F. Kaplan, T. Xu, and L. J. Guo, “High efficiency resonance-based spectrum filters with tunable transmission bandwith fabricated using nanoimprint lithography,” Appl. Phys. Lett. 99(14), 143111 (2011).

[44] C. H. Park, Y. T. Yoon, and S. S. Lee, “Polarization-independent visible wavelength filter incorporating symmetric metal-dielectric resonant structure,” Opt. Express 20(21), 23769-23777 (2012).

[45] C. H. Park, Y. T. Yoon, V. R. Shrestha, C. S. Park, S. S. Lee, and E. S. Kim, “Electrically tunable color filter based on a polarization-tailored nano-photonic dichroic resonator featuring an asymmetric subwavelength grating,” Opt. Express 21(23), 28783-28793 (2013).

[46] V. R. Shrestha, C. S. Park, and S. S. Lee, “Enhancement of color saturation and color gamut enabled by a dual-band color filter exhibiting an adjustable spectral response,” Opt. Express 22(3), 3691-3704 (2014).

Chapter 4

[1] R. Brendel, *Thin-film crystalline silicon solar cells: physics and technology*, John Wiley & Sons, 2011.

[2] A. V. Shah, et al. "Thin-film silicon solar cell technology." Progress in photovoltaics: Research and applications 12.2-3, 113-142 (2004).

[3] J. Müller, et al. "TCO and light trapping in silicon thin film solar cells." Solar energy 77.6, 917-930 (2004).

[4] M. Niggemann, et al. "Diffraction gratings and buried nano-electrodes—architectures for organic solar cells." Thin Solid Films 451, 619-623 (2004).

[5] J. Gjessing, E. S. Marstein, and A. Sudbø. "2D back-side diffraction grating for improved light trapping in thin silicon solar cells." Optics express 18.6, 5481-5495 (2010).

[6] W. Wu, and R. Magnusson. "Total absorption of TM polarized light in a 100 nm spectral band in a nanopatterned thin a-Si film." Optics letters 37.11, 2103-2105 (2012).

[7] T. Khaleque, and R. Magnusson. "Light management through guided-mode resonances in thin-film silicon solar cells." Journal of Nanophotonics 8.1, 083995-083995 (2014).

[8] S. S. Wang, and R. Magnusson. "Theory and applications of guided-mode resonance filters." Applied optics 32.14, 2606-2613 (1993).

[9] S. Tibuleac, and R. Magnusson. "Reflection and transmission guided-mode resonance filters." JOSA A 14.7, 1617-1626 (1997).

[10] R. Magnusson, et al. "Resonant photonic biosensors with polarization-based multiparametric discrimination in each channel." Sensors 11.2, 1476-1488 (2011).

[11] A. L. Fannin, et al. "Experimental evidence for coherent perfect absorption in guided-mode resonant silicon films." IEEE Photonics Journal 8.3, 1-7 (2016).

[12] S. Enoch, and N. Bonod, eds. *Plasmonics: from basics to advanced topics*. Vol. 167. Springer, 2012.

[13] J. M. McMahon, et al. "Tailoring the sensing capabilities of nanohole arrays in gold films with Rayleigh anomaly-surface plasmon polaritons." Optics express 15.26, 18119-18129 (2007).

[14] Y. H. Ko, M. Shokooh-Saremi, and R. Magnusson. "Modal Processes in Two-Dimensional Resonant Reflectors and Their Correlation with Spectra of One-Dimensional Equivalents." IEEE Photonics Journal 7.5, 1-10 (2015).

[15] A. F. i Morral, P. R. i Cabarrocas, and C. Clerc. "Structure and hydrogen content of polymorphous silicon thin films studied by spectroscopic ellipsometry and nuclear measurements." Physical Review B 69.12, 125307 (2004).

[16] E. D. Palik, *Handbook of optical constants of solids*. Vol. 3. Academic press, 1998.

[17] J. Seo, et al. "Nanopatterning by laser interference lithography: applications to optical devices." Journal of nanoscience and nanotechnology 14.2, 1521-1532 (2014).

[18] A. Shah, et al. "Photovoltaic technology: the case for thin-film solar cells." Science 285.5428, 692-698 (1999).

Chapter 5

[1] G. W. Stroke, and D. Gabor. "An introduction to coherent optics and holography," Science Progress (1933-), vol. 55, no. 218, 317-319 (1967).

[2] M. Bass, et al., eds. *Handbook of optics*. Vol. 2. New York: McGraw-Hill, 2001.

[3] E. Hecht, *Optics, 4th Edition*, Pearson, 2002.

[4] D. L. White and G. N. Taylor, "New absorptive mode reflective liquid-crystal display device." Journal of Applied Physics 45.11, 4718-4723 (1974).

[5] K. Aydin, et al. "Broadband polarization-independent resonant light absorption using ultrathin plasmonic super absorbers." Nature communications 2, 517 (2011).

[6] S. Enoch, and N. Bonod, *Plasmonics: from basics to advanced topics*. Vol. 167. Springer, 2012.

[7] N. Liu, et al. "Infrared perfect absorber and its application as plasmonic sensor." Nano letters 10.7, 2342-2348 (2010).

[8] M. K. Hedayati, et al. "Design of a perfect black absorber at visible frequencies using plasmonic metamaterials," Advanced Materials 23.45, 5410-5414 (2011).

[9] L. Meng, D. Zhao, Z. Ruan, Q. Li, Y. Yang, and M. Qiu, "Optimized grating as an ultra-narrow band absorber or plasmonic sensor," Opt. Lett. 39, 1137-1140 (2014).

[10] C. Wu, et al. "Large-area wide-angle spectrally selective plasmonic absorber." *Physical Review B* 84.7, 075102 (2011).

[11] H. Hertz, *Electric Waves* (Macmillan and Company, Ltd., London, 1893), p. 177. First use of a wire grid polarizer.

[12] T. Weber, S. Kroker, T. Käsebier, E. Kley, and A. Tünnermann, "Silicon wire grid polarizer for ultraviolet applications," Appl. Opt. 53, 8140-8144 (2014).

[13] G. R. Bird and M. Parrish, "The Wire Grid as a Near-Infrared Polarizer," J. Opt. Soc. Am. 50, 886-891 (1960).

[14] W. Kern, *Thin film processes II*. Vol. 2. Academic press, 2012.

[15] J. Hägglund and F. Sellberg, "Reflection, Absorption, and Emission of Light by Opaque Optical Gratings," J. Opt. Soc. Am. 56, 1031-1040 (1966).

[16] E. Popov, D. Maystre, R.C. McPhedran, M. Nevière, M.C. Hutley, and G.H Derrick, "Total absorption of unpolarized light by crossed gratings," Opt. Express 16, 6146-6155 (2008).

[17] D. L. Brundrett, T. K. Gaylord, and E. N. Glytsis, "Polarizing mirror/absorber for visible wavelengths based on a silicon subwavelength grating: design and fabrication," Appl. Opt. 37, 2534-2541 (1998).

[18] C. M. Watts, X. Liu, and W. J. Padilla. "Metamaterial electromagnetic wave absorbers," Advanced materials 24.23 (2012).

[19] S. S. Wang and R. Magnusson, "Theory and applications of guided-mode resonance filters," Appl. Opt. 32, 2606-2613 (1993).

[20] D. Wawro, S. Tibuleac, R. Magnusson, and H. Liu, “Optical fiber endface biosensor based on resonances in dielectric waveguide gratings,” Proc. SPIE 3911 (2000).

[21] R. Magnusson, M. Niraula, J. W. Yoon, Y. H. Ko, and K. J. Lee, “Guided-mode resonance nanophotonics in materially sparse architectures,” Proc. SPIE 9757, 975705 (2016).

[22] T. Khaleque and R. Magnusson, “Light management through guided-mode resonances in thin-film silicon solar cells,” J. Nanophotonics, 8(1), 083995-083995 (2014).

[23] M. G. Moharam, et al. "Formulation for stable and efficient implementation of the rigorous coupled-wave analysis of binary gratings." JOSA a 12.5, 1068-1076 (1995).

[24] Z. Huang, et al. "Metal-assisted chemical etching of silicon: a review." *Advanced materials* 23.2, 285-308 (2011).

[25] H. Miao, et al. "Cryogenic etching of high aspect ratio 400-nm pitch silicon gratings." Journal of Microelectromechanical Systems 25.5, 963-967 (2016).

Chapter 6

[1] V. C. Lopes, A. J. Syllaios, and M. C. Chen. "Minority carrier lifetime in mercury cadmium telluride." Semiconductor Science and Technology 8.6S, 824 (1993).

[2] M. Kopytko, and A. Rogalski. "HgCdTe barrier infrared detectors." Progress in Quantum Electronics 47, 1-18 (2016).

[3] M. S. Gudiksen, et al. "Growth of nanowire superlattice structures for nanoscale photonics and electronics." Nature 415.6872, 617-620 (2002).

[4] J. R. Janesick, *Photon transfer*. San Jose: SPIE press, 2007.

[5] M. A. Green, *Solar cells: operating principles, technology, and system applications*, Prentice Hall, 1982.

[6] J. Hu, and R. G. Gordon. "Textured fluorine-doped ZnO films by atmospheric pressure chemical vapor deposition and their use in amorphous silicon solar cells." Solar cells 30.1-4, 437-450 (1991).

[7] K. L. Chopra, and S. R. Das, *Thin film solar cells*. Springer Science & Business Media, 2013.

[8] M. D. Goldflam, et al. "Enhanced infrared detectors using resonant structures combined with thin type-II superlattice absorbers." Applied Physics Letters 109.25, 251103 (2016).

[9] R. Magnusson, and S. S. Wang. "Optical guided-mode resonance filter." U.S. Patent No. 5,216,680. 1 Jun. 1993.

[10] Z. S. Liu, et al. "High-efficiency guided-mode resonance filter." Optics letters 23.19, 1556-1558 (1998).

[11] T. Khaleque and R. Magnusson. "Light management through guided-mode resonances in thin-film silicon solar cells." Journal of Nanophotonics 8.1, 083995-083995 (2014).

Chapter 7

[1] M. T. Do, Q. C. Tong, A. Lidiak, et al, “Fabrication and characterization of large-area unpatterned and patterned plasmonic gold nanostructures,” Appl. Phys. A, 122-360 (2016).

[2] A. Cunningham, et al. "Coupling of plasmon resonances in tunable layered arrays of gold nanoparticles." The Journal of Physical Chemistry C115.18, 8955-8960 (2011).

[3] J. W. Yoon, K. J. Lee, W. Wu, and R. Magnusson, “Wideband omnidirectional polarization-insensitive light absorbers made with 1D silicon gratings,” Advanced Optical Materials 2, 1206-1212 (2014).

Biographical information

Alex Fannin completed his B.S.E.E. at UT Arlington in 2012 graduating with honors. Prior to graduation he joined both Eta Kappa Nu and Tau Beta Pi. He began his Ph.D. work at UT Arlington in the fall of 2012 studying wireless power transfer. In 2013, he changed his focus to optical engineering and begun studying guided-mode resonant topologies. His current work involves the study of absorptive properties in guided-mode resonant thin films.

In the summer of 2013 he formed his first company, AOS Enterprises, to accumulate business knowledge and experience for future endeavors and education. His time working on AOS directly lead to the pursuit of an MBA that started in the winter of 2015 at Western Governors University. He intends to finish his business education in November of 2017.

Alex's current interests include the design and fabrication of efficient light harvesting materials applicable in large scale, cost effective manufacturing processes. His goal is to join an industry focused on the design and fabrication of such devices where he may leverage both his technological and business backgrounds to bring forth highly efficient, low cost, and consumer friendly goods.